

Abstract

AITKEN, MATTHEW LAWRENCE. Lidar-Aided Inertial Navigation with Extended Kalman Filtering for Pinpoint Landing. (Under the direction of Dr. Robert H. Tolson.)

In support of NASA's Autonomous Landing and Hazard Avoidance Technology project, an extended Kalman filter (EKF) routine has been developed for estimating the position, velocity, and attitude of a spacecraft during the landing phase of a planetary mission. The EKF is a recursive algorithm for obtaining the minimum variance estimate of a nonlinear dynamic process from a sequence of noisy observations. The proposed filter combines measurements of acceleration and angular velocity from an inertial measurement unit with range and range-rate observations from an onboard light detection and ranging (LIDAR) system. These high-precision LIDAR measurements of distance to the ground and approach velocity will enable both robotic and manned vehicles to land safely and precisely at scientifically interesting sites. The robustness and accuracy of the Kalman filter were first established using a simplified simulation of the final translation and touchdown phase of the Apollo lunar landings. In addition, experimental results from a helicopter flight test performed at NASA Dryden in August 2008 demonstrate the merit in employing LIDAR for pinpoint landing in future space missions.

Lidar-Aided Inertial Navigation with Extended Kalman Filtering for Pinpoint Landing

by
Matthew Lawrence Aitken

A thesis submitted to the Graduate Faculty of
North Carolina State University
in partial fulfillment of the
requirements for the Degree of
Master of Science

Aerospace Engineering

Raleigh, NC

2009

APPROVED BY:

Fred DeJarnette

Andre Mazzoleni

Robert Tolson
Chair of Advisory Committee

Dedication

For Michelle

Biography

Matthew L. Aitken was born in 1984 in White Plains, New York and attended public schools in Chapel Hill, North Carolina, where he also received a Bachelor of Science in Physics from the University of North Carolina in 2006. After graduating, he worked for one year as a software developer at Intelligent Information Systems in Research Triangle Park (Durham, North Carolina). In May 2007, he began study for a Master of Science in Aerospace Engineering at North Carolina State University in Raleigh, North Carolina, where he was also a graduate research assistant in the Department of Mechanical and Aerospace Engineering until the end of that year. He has been employed in that same position, working in residence at both NASA Langley Research Center and the National Institute of Aerospace in Hampton, Virginia, since January 2008. Beginning in August 2009, he plans to pursue a Doctor of Philosophy in Physics at the University of Colorado.

Acknowledgements

There are many people I wish to thank, the first of whom is my adviser, Dr. Robert Tolson. His steady support, extensive experience, and insightful interpretations were invaluable to the completion of this work. Both his guidance and technical contributions are greatly appreciated. Special thanks also to Dr. Fred DeJarnette and Dr. Andre Mazzoleni for their many helpful comments and for agreeing to serve on my committee.

In addition, I would particularly like to thank the principal investigator of this project, Dr. Farzin Amzajerjian of NASA Langley Research Center, for his sponsorship and continuous encouragement. I am deeply indebted to Diego Pierrottet of Coherent Applications, Inc. and Jason Keim of Jet Propulsion Laboratory for their generous provision of and assistance with the test data, without which this undertaking would have been impossible.

I also want to sincerely thank my family, for I would not be here without them. As my Mom would say, “I brought you into this world, and I can take you out.” I am fortunate to have two remarkable brothers, Myles and Graham, who always remind me of the humor and joy in life. I am most grateful to my grandparents for their love, backing, and advice throughout my educational career. Thank you Mom and Dad for all that you have bestowed upon me and for being the best parents in the world. Your example is an inspiration for my own life. Most of all, thank you Michelle for your endless care,

support, and devotion. Because of you, I am the luckiest man on the face of the earth.

This work is as much yours as it is mine. I love all of you very much.

Table of Contents

List of Figures.....	vii
Nomenclature and Abbreviations	viii
1 Preface	1
2 Inertial Navigation.....	3
3 Coordinate Systems	6
4 The Extended Kalman Filter	9
4.1 Prediction	10
4.2 Filtering	11
5 Sensor Models.....	13
5.1 Inertial Measurement Unit	13
5.2 LIDAR Measurement Model.....	14
6 Estimator Description	17
6.1 Attitude Kinematics	17
6.2 The State Equation.....	18
6.3 State Error Model	20
6.4 Measurement Sensitivity Matrix	23
6.5 Update and Propagation	25
7 Simulation Results	27
7.1 Model	28
7.2 Discussion	29
8 Experimental Results	42
8.1 Model	42
8.2 Discussion	46
9 Conclusion and Future Work	61
References.....	63

List of Figures

Figure 5.1: LIDAR system geometry	15
Figure 5.2: Linear frequency modulation.	16
Figure 7.1: History of position estimate and uncertainty without LIDAR.	32
Figure 7.2: History of position estimate and uncertainty with LIDAR.	33
Figure 7.3: History of velocity estimate and uncertainty without LIDAR.	34
Figure 7.4: History of velocity estimate and uncertainty with LIDAR.	35
Figure 7.5: History of accel bias estimate and uncertainty without LIDAR.	36
Figure 7.6: History of accel bias estimate and uncertainty with LIDAR.	37
Figure 7.7: History of gyro bias estimate and uncertainty without LIDAR.	38
Figure 7.8: History of gyro bias estimate and uncertainty with LIDAR.	39
Figure 7.9: History of attitude estimate and uncertainty without LIDAR.	40
Figure 7.10: History of attitude estimate and uncertainty with LIDAR.	41
Figure 8.1: Flight test helicopter	43
Figure 8.2: Ground track of helicopter as measured by GPS.	47
Figure 8.3: Altitude above surface versus time as measured by GPS.	47
Figure 8.4: Position estimate and residual versus time without LIDAR.	51
Figure 8.5: Position estimate and residual versus time with LIDAR.	52
Figure 8.6: Velocity estimate and residual versus time without LIDAR.	53
Figure 8.7: Velocity estimate and residual versus time with LIDAR.	54
Figure 8.8: Accelerometer bias estimate and uncertainty versus time without LIDAR.	55
Figure 8.9: Accelerometer bias estimate and uncertainty versus time with LIDAR.	56
Figure 8.10: Gyro bias estimate and uncertainty time without LIDAR.	57
Figure 8.11: Gyro bias estimate and uncertainty versus time with LIDAR.	58
Figure 8.12: Attitude estimate and residual versus time without LIDAR.	59
Figure 8.13: Attitude estimate and residual versus time with LIDAR.	60

Nomenclature and Abbreviations

Vectors are represented by boldface characters. All vectors are 3×1 , and all matrices are 3×3 , unless otherwise indicated.

Symbols

A	rotation from navigation frame to vehicle body frame
\mathbf{a}	net body acceleration
\mathbf{a}_m	measured net body acceleration
B	modulation bandwidth of laser signal
\mathbf{b}_a	accelerometer drift-rate bias
\mathbf{b}_g	gyroscope drift-rate bias
c	speed of light
F	continuous-time state transition matrix (15×15)
f_d	Doppler shift frequency
G	input noise sensitivity matrix (15×12)
\mathbf{g}	gravitational acceleration
GM	universal gravitational constant multiplied by the mass of the Earth
H	measurement sensitivity matrix (6×15)
K	Kalman gain matrix (15×6)
L	matrix whose columns are the direction cosines of the 3 LIDAR beams in the vehicle body frame
N	discrete-time state noise covariance matrix (15×15)
\mathbf{n}_a	accelerometer drift-rate noise
\mathbf{n}_g	gyroscope drift-rate noise
\mathbf{n}_{ra}	accelerometer drift-rate ramp noise
\mathbf{n}_{rg}	gyroscope drift-rate ramp noise
P	state error covariance matrix (16×16)
\tilde{P}	reduced-dimension covariance matrix (15×15)
P_0	initial covariance (16×16)
P_k^-	predicted covariance at time t_k (16×16)
P_k^+	updated covariance following measurement at time t_k (16×16)
\mathbf{p}	position
Q	continuous-time state noise covariance matrix (12×12)
q	attitude quaternion

R	measurement noise covariance matrix (6×6)
R_c^v	rotation from LGCV to LGV
R_e^c	rotation from ECEF to LGCV
R_e^v	rotation from ECEF to LGV
R_i^b	rotation from IMU frame to vehicle body frame
T	waveform period of laser signal
u	measurement noise (6×1)
v	velocity
w	state noise (12×1)
x	state vector (16×1)
\hat{x}	state estimate (16×1)
\tilde{x}	reduced-dimension state vector (15×1)
x_0	initial state estimate (16×1)
\hat{x}_k^-	predicted state estimate at time t_k (16×1)
\hat{x}_k^+	updated state estimate following measurement at time t_k (16×1)
z	measurement vector (6×1)
Δx	state error vector (16×1)
δA	direction cosine matrix corresponding to quaternion error δq
δq	quaternion error
$\delta \theta$	infinitesimal attitude error angle vector
Λ	longitude
λ	laser wavelength
ρ	range (distance to the ground)
$\dot{\rho}$	range-rate (line-of-sight velocity)
Φ	discrete-time state transition matrix (15×15)
φ	geodetic latitude
φ_c	geocentric latitude
ω	body angular velocity
ω_e	angular velocity of the Earth
ω_m	measured body angular velocity

Subscripts

a	accelerometer
d	Doppler
e	Earth
g	gyroscope
k	value at k -th time step

m	measured value
r	ramp
0	initial value

Superscripts

b	vehicle body frame
c	LGCV frame
e	ECEF frame
i	IMU frame
v	LGV frame
-	predicted value
+	updated value

Abbreviations

ECEF	Earth-centered Earth-fixed
EKF	extended Kalman filter
GPS	Global Positioning System
IERS	International Earth Rotation and Reference Systems Service
IMU	inertial measurement unit
JPL	Jet Propulsion Laboratory
LGCV	local geocentric vertical
LGV	local geodetic vertical
LIDAR	light detection and ranging
WGS 84	World Geodetic System of 1984

1 Preface

Future space exploration will require that descent vehicles employ accurate real-time state estimation, enabling the capability to land precisely and safely at scientifically promising but potentially hazardous sites. Robotic exploration, sample return, and human missions to the Moon, Mars, and other bodies in the solar system warrant the development of sophisticated hazard avoidance and precision landing technologies. Pinpoint landing will be particularly vital for human exploration vehicles, which will need to land proximate to pre-positioned supplies and emergency abort systems.

Taking Mars for example, the estimated landing accuracy for Mars Pathfinder, which landed on the red planet in 1997, was within 150 km of the intended target. Due to improvements in approach navigation, namely more accurate models of the upper Martian atmosphere, the estimated landing accuracy was reduced to 35 km for the Mars Exploration Rovers in 2004. Mars Science Laboratory, scheduled to be launched in 2011, is expected to land within 10 km of the target (Amzajerjian). However, by relying on existing technologies, such as radar altimeters and motion estimation cameras, significant gains in landing accuracy will be seriously limited by uncertainties in the middle Martian atmosphere. Thus, current state of the art is inadequate for targeting and safely landing at scientifically interesting sites, which typically contain hazardous terrain features, such as craters, slopes, and rocks.

For this reason, the development of a more capable and robust landing system, featuring a light detection and ranging (LIDAR)-based autonomous guidance and control

instrument, is essential for reducing risks and increasing performance of future planetary missions. The flight-qualified version of this technology is anticipated to have the capability of navigating to within 10 to 100 m of the target by analyzing terrain features and identifying safe landing sites. Moreover, the system will provide real-time trajectory updates, in particular surface proximity, orientation, and vector velocity. Two laser sensors are employed to meet these objectives: a three-dimensional imaging LIDAR to provide surface topography information and a coherent range and velocity LIDAR to provide precision altitude, velocity, and attitude updates. Demonstrating the ability of the range and velocity LIDAR to estimate the state of the vehicle is the subject of this report.

To accomplish this task, an extended Kalman filter (EKF) has been developed to estimate position, velocity, and attitude during landing. The proposed estimator combines measurements of acceleration and angular velocity from an inertial measurement unit (IMU) with range and range-rate observations from an onboard LIDAR system. Data from a helicopter flight test carried out at NASA Dryden in August 2008 was used to evaluate system performance. Analysis of the results shows filter estimates in excellent agreement with high-accuracy GPS measurements. Appropriate reviews of inertial navigation, coordinate systems, and nonlinear state estimation using extended Kalman filtering are provided prior to the discussion of results. The sections on inertial navigation and coordinate systems are taken largely from Chatfield, while Lefferts et al. provide much of the material found in the EKF overview.

In the sections that follow, vectors are represented by boldface characters. Vector magnitudes are indicated by the vector symbol in regular type. Derivatives are written

using standard engineering notation: a single dot denotes the first derivative with respect to time, while a double dot denotes the second derivative with respect to time. The primary system of units used here is the mks system, i.e. length is measured in meters (m), mass in kilograms (kg), and time in seconds (s). Accordingly, velocity is measured in m/s and acceleration in m/s^2 . To be consistent with these units, angular velocity would be expressed in radians per second (rad/s); however, the angular rates encountered in inertial navigation are usually much less than 1 rad/s. For this reason, angular rate, especially gyroscope drift, is often expressed in degrees per hour (deg/hr).

2 Inertial Navigation

Inertial navigation involves the estimation of the position, velocity, and orientation of a moving body and has numerous applications in both atmospheric and space flight. The primary sensors used in inertial navigation systems are the gyroscope and accelerometer, which measure the angular velocity and acceleration due to non-gravitational forces, respectively, of the body with respect to inertial space. These two instruments are collectively referred to as the inertial measurement unit. While the initial state is usually provided by an external source, such as GPS, independent updates to the state can be obtained by integrating the rates provided by the inertial sensors.

However, even the most advanced inertial navigation systems suffer from integration drift; by themselves, accelerometers and gyroscopes provide changes to the

state with ever-increasing error. For this reason, IMU data is often combined with external measurements to improve navigation accuracy. In this case, the process is referred to as *aided* inertial navigation. Specifically, this report examines the use of LIDAR range and range-rate observations in supplementing the measurements provided by the IMU.

A central discipline within the field of inertial navigation is geodesy, which involves the measurement and representation of the Earth's shape and gravitational field. For bodies near the surface of the Earth, acceleration due to gravity is particularly sensitive to variations in location because of the non-spherical shape and non-uniformly distributed mass density of the Earth. In such applications, sophisticated gravity models are critical for high-accuracy inertial navigation.

Consider a vehicle with position \mathbf{p} with respect to an inertial coordinate system whose origin is the center of the Earth. According to Newton's universal law of gravitation, the gravitational acceleration due to the attraction of a spherical, homogeneous Earth is given by

$$\mathbf{g} = -\frac{GM}{p^3} \mathbf{p} \quad (2.1)$$

where GM is the product of the universal gravitational constant and the mass of the Earth. Due to local gravity anomalies and other factors, such as the oblateness of the Earth, gravity is almost always more complex than this simple central force field.

Airborne vehicles near the surface of the Earth are subject to gravity in addition to other forces, the most common of which are thrust, lift, and drag. Non-gravitational force

per unit mass is often referred to as specific force. From Newton's second law, the acceleration of such a vehicle is given by

$$\ddot{\mathbf{p}} = \mathbf{a} = \mathbf{a}_m + \mathbf{g} \quad (2.2)$$

where \mathbf{a}_m is the net specific force. (Here, the subscript m has been used because \mathbf{a}_m is the net acceleration measured by the accelerometer. Also, all vectors in Equation (2.2) are understood to be in the inertial coordinate system.) Equation (2.2), which states that the total kinematic acceleration of a body is equal to the sum of the specific force and gravitational acceleration, is the fundamental equation for inertial navigation in inertial coordinates. When the navigation coordinate system is non-inertial, the right hand side of the equation includes additional terms, which will be encountered in Section 6.2.

Equation (2.2) is valid even if the actual gravity differs from the central term represented by Equation (2.1).

With a mathematical model of the gravity field and IMU measurements of the specific force, the velocity \mathbf{v} is calculated as the sum of the initial velocity and the integral over time of the kinematic acceleration

$$\mathbf{v} = \mathbf{v}_0 + \int \mathbf{a} dt \quad (2.3)$$

Similarly, position is found by adding the initial position to the integral over time of the velocity

$$\mathbf{p} = \mathbf{p}_0 + \int \mathbf{v} dt \quad (2.4)$$

In addition to determining translational motion, inertial navigation systems employ gyroscopes for sensing the angular velocity of a body with respect to inertial

space. Just as accelerometer measurements are used to integrate the kinematic equations for position and velocity, angular rates are used to integrate the kinematic equation for attitude. Often, quaternions are used to represent the orientation of the vehicle. Attitude dynamics and the quaternion kinematic equation are treated in greater detail in Section 6.1.

3 Coordinate Systems

Navigation systems measure acceleration and angular velocity with respect to inertial space, but position, velocity, and orientation are often expressed in terms of Earth-based, non-inertial coordinate systems. Thus, coordinate systems and coordinate transformations are fundamental concepts in inertial navigation. The coordinate systems described in this section are orthogonal and are defined by specifying the location of the origin and the direction of three axes.

In particular, the World Geodetic System is a standard for use in navigation which models the Earth as an oblate spheroid with an elliptical cross section to closely approximate mean sea level. The system also defines a standard Earth-centered Earth-fixed (ECEF) coordinate frame which rotates with angular velocity ω_e equal to the true rotation rate of the Earth. The center of the reference ellipsoid and origin of the coordinate frame are designed to coincide with the Earth's center of mass. The z -axis of the ECEF frame points from the origin to the north pole. The x -axis lies in the plane of

the Earth's equator and points towards the International Earth Rotation and Reference Systems Service (IERS) reference meridian—5.31 arcseconds east of the Greenwich prime meridian—and the y -axis completes the right-handed system. The latest model, the World Geodetic System of 1984 (WGS 84), is the coordinate system used by the Global Positioning System (GPS). WGS 84 defines $GM = 3.986005 \times 10^{14} \text{ m}^3/\text{s}^2$ and $\omega_e = 7.292115 \times 10^{-5} \text{ rad/s}$. When necessary, vectors in the ECEF frame are denoted by a superscript e .

Position and velocity are often expressed in the local geodetic vertical (LGV) or geographic coordinate system, in which the z -axis is everywhere normal to the Earth reference ellipsoid. The x - and y -axes are directed toward geographic north and west, respectively. The local geocentric vertical (LGCV) frame is similar to the LGV frame, except that the z -axis is coincident with a line from the center of the Earth to the point of interest. Like the ECEF frame, the origin of the LGV and LGCV frames is the Earth center of mass. When necessary, vectors in the LGV and LGCV frames will be indicated by the superscripts v and c , respectively.

The origin of the vehicle body coordinate system is taken to be the IMU center of mass. The x -axis, which corresponds to the vehicle roll axis, points forward along the longitudinal axis of the vehicle. The y -axis (pitch axis) is directed 90 degrees to the left when facing forward, normal to the roll axis. The z -axis (yaw axis) is directed upward normal to the xy -plane. The IMU input axes, whose origin is also the IMU center of mass, do not necessarily correspond to the body-fixed axes. When necessary, the letter b will be

used to denote the body-fixed coordinate system, while the letter i will be used to denote the IMU input coordinate frame.

As would be expected, transformations between the different types of coordinate systems are frequently required. Transformations between orthogonal frames are rotations and are designated by the direction cosine matrix R with appropriate subscript and superscript. Rotations map vectors in the subscript system to the superscript system.

For example, take the position vector of a point in the LGV frame to be $\mathbf{p}^v = [p_x \ p_y \ p_z]^T$. Because the rotation from the LGCV frame to the LGV frame is small, the corresponding transformation is closely approximated by the skew-symmetric matrix

$$R_c^v = \frac{1}{p} \begin{bmatrix} p_z & 0 & p_x \\ 0 & p & 0 \\ -p_x & 0 & p_z \end{bmatrix} \quad (3.1)$$

where it should be noted that R_c^v is not orthonormal. Denoting longitude and geodetic latitude Λ and φ , respectively, the rotation from ECEF to LGV is given by

$$R_e^v = \begin{bmatrix} -\cos \Lambda \sin \varphi & -\sin \Lambda \sin \varphi & \cos \varphi \\ \sin \Lambda & -\cos \Lambda & 0 \\ \cos \Lambda \cos \varphi & \sin \Lambda \cos \varphi & \sin \varphi \end{bmatrix} \quad (3.2)$$

Finally, to obtain the rotation from ECEF to LGCV, geodetic latitude is replaced with geocentric latitude φ_c in Equation (3.2)

$$R_e^c = \begin{bmatrix} -\cos \Lambda \sin \varphi_c & -\sin \Lambda \sin \varphi_c & \cos \varphi_c \\ \sin \Lambda & -\cos \Lambda & 0 \\ \cos \Lambda \cos \varphi_c & \sin \Lambda \cos \varphi_c & \sin \varphi_c \end{bmatrix} \quad (3.3)$$

4 The Extended Kalman Filter

The Kalman filter is a recursive algorithm that estimates the state of a linear dynamic system from a series of noisy measurements; moreover, state noise is used to model uncertain system parameters. Its nonlinear counterpart, the *extended* Kalman filter, is a non-optimal estimator which linearizes about the current state estimate. Despite the inaccuracy introduced by this approximation scheme, the extended Kalman filter is a standard in navigation systems. Following the notation of Lefferts et al., the general system is governed by the state equation

$$\frac{d}{dt} \mathbf{x}(t) = \mathbf{f}(\mathbf{x}(t), t) + \mathbf{g}(\mathbf{x}(t), t)\mathbf{w}(t) \quad (4.1)$$

where $\mathbf{x}(t)$ is the state vector and the vector $\mathbf{w}(t)$ is Gaussian white noise whose mean and covariance are given by

$$E[\mathbf{w}(t)] = \mathbf{0} \quad (4.2)$$

$$E[\mathbf{w}(t)\mathbf{w}^T(t')] = \mathbf{Q}(t)\delta(t-t') \quad (4.3)$$

where E denotes expectation value. The initial mean and covariance of the state vector are given by

$$E[\mathbf{x}(t_0)] \equiv \hat{\mathbf{x}}(t_0) = \mathbf{x}_0 \quad (4.4)$$

$$E[(\mathbf{x}(t_0) - \mathbf{x}_0)(\mathbf{x}(t_0) - \mathbf{x}_0)^T] \equiv \mathbf{P}(t_0) = \mathbf{P}_0 \quad (4.5)$$

4.1 Prediction

In the absence of any measurements, the minimum variance estimate of the state at time t is given by the conditional expectation

$$\hat{\mathbf{x}}(t) = E[\mathbf{x}(t) | \mathbf{x}_0] \quad (4.6)$$

The predicted estimate satisfies the differential equation

$$\frac{d}{dt} \hat{\mathbf{x}}(t) = E[\mathbf{f}(\mathbf{x}(t), t)] \equiv \hat{\mathbf{f}}(\mathbf{x}(t), t) \approx \mathbf{f}(\hat{\mathbf{x}}(t), t) \quad (4.7)$$

which can be integrated to yield

$$\hat{\mathbf{x}}(t) = \boldsymbol{\varphi}(t, \hat{\mathbf{x}}(t_0), t_0) \quad (4.8)$$

The state error vector and the corresponding covariance matrix can be written as

$$\Delta \mathbf{x}(t) = \mathbf{x}(t) - \hat{\mathbf{x}}(t) \quad (4.9)$$

$$P(t) = E[\Delta \mathbf{x}(t) \Delta \mathbf{x}^T(t)] \quad (4.10)$$

Applying a first-order Taylor series expansion about the state estimate to Equation (4.1)

$$\begin{aligned} \frac{d}{dt} \mathbf{x}(t) &\approx \mathbf{f}(\hat{\mathbf{x}}(t), t) + \left. \frac{\partial}{\partial \mathbf{x}} \mathbf{f}(\mathbf{x}, t) \right|_{\hat{\mathbf{x}}(t)} \Delta \mathbf{x}(t) + g(\hat{\mathbf{x}}(t), t) \mathbf{w}(t) \\ &= \mathbf{f}(\hat{\mathbf{x}}(t), t) + F(t) \Delta \mathbf{x}(t) + G(t) \mathbf{w}(t) \end{aligned}$$

Using Equations (4.7) and (4.9), it is readily seen that the state error vector satisfies the differential equation

$$\frac{d}{dt} \Delta \mathbf{x}(t) = F(t) \Delta \mathbf{x}(t) + G(t) \mathbf{w}(t) \quad (4.11)$$

which may be integrated to give

$$\Delta \mathbf{x}(t) = \Phi(t, t_0) \Delta \mathbf{x}(t_0) + \int_{t_0}^t \Phi(t, t') G(t') \mathbf{w}(t') dt' \quad (4.12)$$

where $\Phi(t, t_0)$ is the state transition matrix, satisfying the differential equation

$$\frac{\partial}{\partial t} \Phi(t, t_0) = F(t)\Phi(t, t_0) \quad (4.13)$$

with the initial condition

$$\Phi(t_0, t_0) = I \quad (4.14)$$

The predicted covariance matrix satisfies the matrix Riccati equation

$$\frac{d}{dt} P(t) = F(t)P(t) + P(t)F^T(t) + G(t)Q(t)G^T(t) \quad (4.15)$$

which may be integrated to yield

$$\begin{aligned} P(t) &= \Phi(t, t_0)P(t_0)\Phi^T(t, t_0) + \int_{t_0}^t \Phi(t, t')G(t')Q(t')G^T(t')\Phi^T(t, t')dt' \\ &= \Phi(t, t_0)P(t_0)\Phi^T(t, t_0) + N(t, t_0) \end{aligned} \quad (4.16)$$

Let $\hat{\mathbf{x}}_k^-$ and P_k^- denote the predicted values of the state vector and the state covariance matrix at time t_k , respectively. Immediately following a measurement at time t_k , these same quantities are denoted by $\hat{\mathbf{x}}_k^+$ and P_k^+ . The state estimate and covariance are mapped to the next measurement time, t_{k+1} , using Equations (4.8) and (4.16):

$$\hat{\mathbf{x}}_{k+1}^- = \boldsymbol{\varphi}(t_{k+1}, \hat{\mathbf{x}}_k^+, t_k) \quad (4.17)$$

$$P_{k+1}^- = \Phi_k P_k^+ \Phi_k^T + N_k \quad (4.18)$$

4.2 Filtering

The measurement vector at time t_k , \mathbf{z}_k , is related to the state by

$$\mathbf{z}_k = \mathbf{h}(\mathbf{x}_k) + \mathbf{u}_k \quad (4.19)$$

where \mathbf{u}_k , the measurement noise, is discrete Gaussian white noise whose mean and covariance are given by

$$E[\mathbf{u}_k] = \mathbf{0} \quad (4.20)$$

$$E[\mathbf{u}_k \mathbf{u}_{k'}^T] = R_k \delta_{kk'} \quad (4.21)$$

Denoting the measurement sensitivity matrix by

$$H_k = \left. \frac{\partial \mathbf{h}(\mathbf{x})}{\partial \mathbf{x}} \right|_{\hat{\mathbf{x}}_k^-} \quad (4.22)$$

and the Kalman gain matrix by

$$K_k = P_k^- H_k^T (H_k P_k^- H_k^T + R_k)^{-1} \quad (4.23)$$

both the estimate and the covariance are updated in a minimum variance sense using the measurement at time t_k

$$\hat{\mathbf{x}}_k^+ = \hat{\mathbf{x}}_k^- + K_k [z_k - \mathbf{h}(\hat{\mathbf{x}}_k^-)] \quad (4.24)$$

$$P_k^+ = (I - K_k H_k) P_k^- (I - K_k H_k)^T + K_k R_k K_k^T \quad (4.25)$$

To summarize, during a single iteration of the filter, the measurement at time t_k is used to correct the predicted values of the state estimate and covariance using Equations (4.24) and (4.25); those quantities are then mapped to the next measurement time, t_{k+1} , using Equations (4.17) and (4.18). The procedure is repeated until no more measurements remain to be processed.

5 Sensor Models

5.1 Inertial Measurement Unit

Following Farrenkopf, both the accelerometer and gyroscope are assumed to be corrupted by a drift-rate bias \mathbf{b} and drift-rate noise \mathbf{n} , the latter of which is modeled as a Gaussian white noise process. To avoid excessive use of subscripts and superscripts, the previous notation for coordinate rotations is abandoned for the transformation from the navigation to the body frame, which will be represented by the matrix A . Thus, the sensor outputs are given by

$$\mathbf{a}_m = A(\mathbf{a} - \mathbf{g}) + \mathbf{b}_a + \mathbf{n}_a \quad (5.1)$$

$$\boldsymbol{\omega}_m = A\boldsymbol{\omega} + \mathbf{b}_g + \mathbf{n}_g \quad (5.2)$$

where $\boldsymbol{\omega}$ is angular velocity of the body in the navigation (planet-fixed) coordinate system. The subscript m in Equations (5.1) and (5.2) denotes the measured value of acceleration and angular velocity, respectively. In both equations, \mathbf{a} , \mathbf{g} , and $\boldsymbol{\omega}$ are understood to be in the navigation frame; all other vectors are understood to be in the vehicle body frame. The subscripts a and g on the bias and noise vectors refer to the accelerometer and gyroscope, respectively.

The drift-rate biases are not constant, but are instead driven by drift-rate ramp noise

$$\frac{d}{dt}\mathbf{b}_a = \mathbf{n}_{ra} \quad (5.3)$$

$$\frac{d}{dt} \mathbf{b}_g = \mathbf{n}_{rg} \quad (5.4)$$

where \mathbf{n}_{ra} and \mathbf{n}_{rg} are assumed to be Gaussian white noise processes. All noise processes are further assumed to be uncorrelated. As in Lefferts et al., IMU data are not treated as observations, and thus IMU noise appears as state noise instead of observation noise. In this case, the system noise vector is written

$$\mathbf{w} = \begin{bmatrix} \mathbf{n}_a \\ \mathbf{n}_{ra} \\ \mathbf{n}_g \\ \mathbf{n}_{rg} \end{bmatrix} \quad (5.5)$$

5.2 LIDAR Measurement Model

In addition to the IMU, the vehicle is also equipped with a LIDAR system containing three telescopes, each of which produces a laser beam directed at a polar angle of 22.5° from the body's negative z -axis; moreover, the three beams are separated azimuthally from each other by angles of 120° (see Figure 5.1). Each LIDAR signal measures distance to the ground (range) ρ_i and line-of-sight velocity (range-rate) $\dot{\rho}_i$, $i = 1, 2, 3$. Thus, the measurement vector \mathbf{z} , which is understood to be in the vehicle body coordinate system, is given by

$$\mathbf{z} = \begin{bmatrix} \rho_1 \\ \rho_2 \\ \rho_3 \\ \dot{\rho}_1 \\ \dot{\rho}_2 \\ \dot{\rho}_3 \end{bmatrix} = \begin{bmatrix} \boldsymbol{\rho} \\ \dot{\boldsymbol{\rho}} \end{bmatrix} \quad (5.6)$$

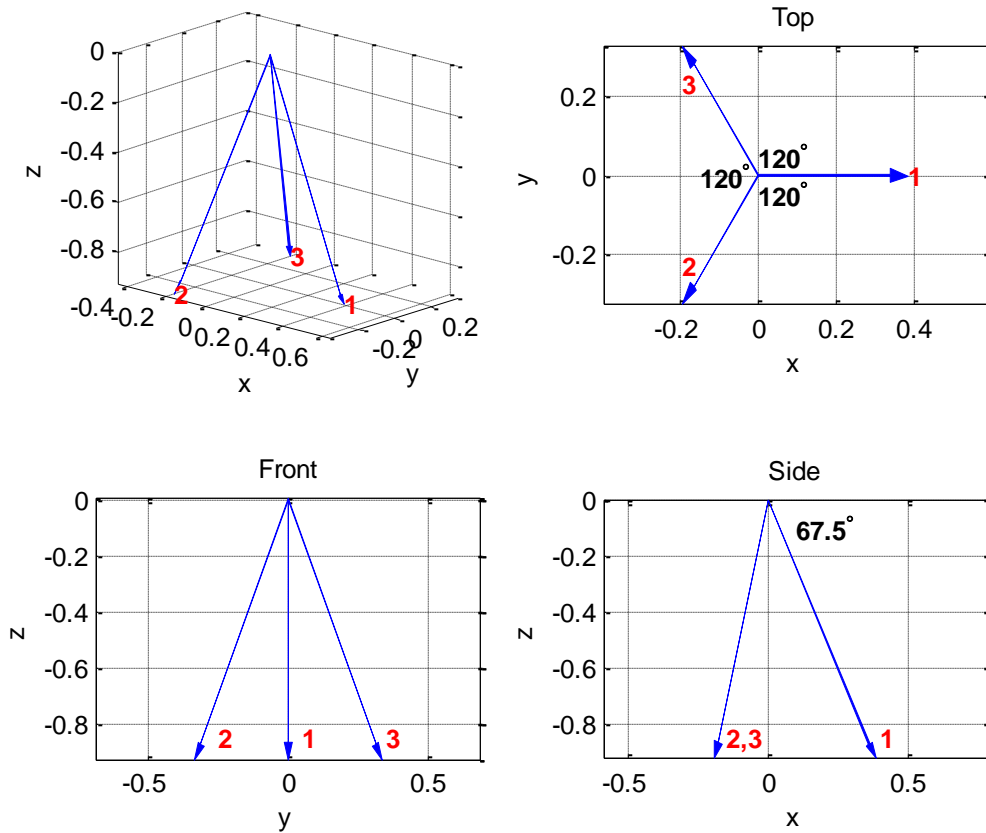


Figure 5.1: LIDAR system geometry

Range and velocity are measured using optical heterodyning (the mixing of two oscillating waveforms) and linear modulation of the laser signal frequency. Unlike radar, the laser beam surface footprint is small (less than 10 cm), which reduces uncertainty in range. Velocity is found by measuring the Doppler shift due to the motion of the vehicle relative to the ground.

Figure 5.2 shows the frequency content of the LIDAR signal versus time. In the figure, T is the waveform period and B is the modulation bandwidth. The transmitted laser beam is reflected from the surface and received by the detector after the round-trip

time of flight $t_a = 2\rho/c$, where ρ is the range to the target and c is the speed of light.

Relative to the outgoing waveform, the incoming signal is horizontally shifted because of this time delay. If the LIDAR platform is moving relative to the ground, the received waveform is also vertically shifted by the frequency f_d due to the Doppler effect. After a little algebra, the target range is easily found to be

$$\rho = \frac{Tc}{4B} f_a \quad (5.7)$$

while the line-of-sight velocity is given by the familiar Doppler effect formula for electromagnetic waves

$$\dot{\rho} = \frac{\lambda f_d}{2} \quad (5.8)$$

where λ is the wavelength of the transmitted wave in the reference frame of the source.

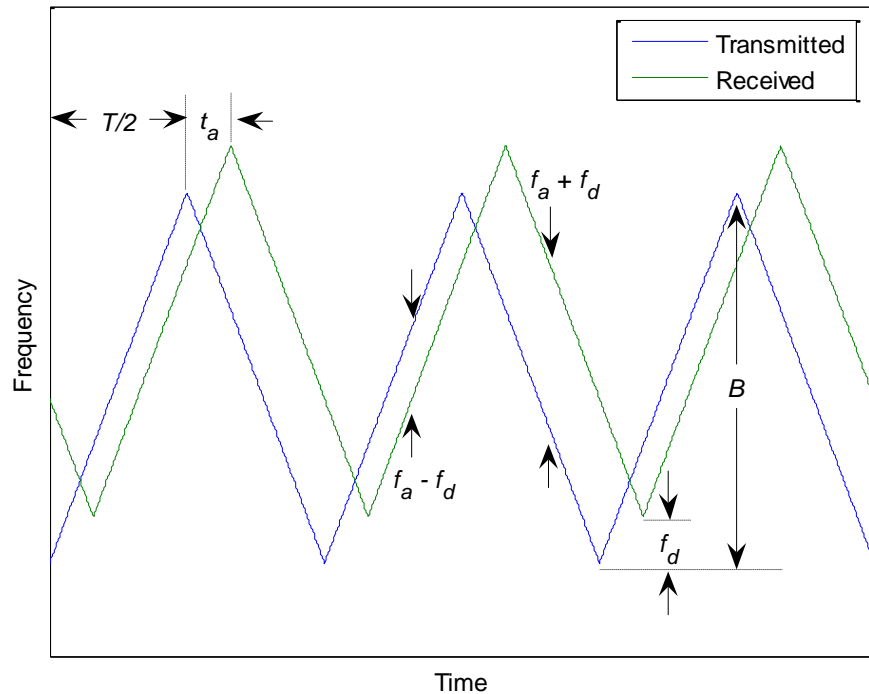


Figure 5.2: Linear frequency modulation.

6 Estimator Description

6.1 Attitude Kinematics

The attitude of the vehicle is represented by the quaternion, defined as

$$q = \begin{bmatrix} \mathbf{q} \\ q_4 \end{bmatrix} \quad (6.1)$$

where $\mathbf{q} = [q_1 \ q_2 \ q_3]^T = \lambda \sin(\theta/2)$ and $q_4 = \cos(\theta/2)$ are the vector and scalar components of the quaternion, respectively. Here, the unit vector λ is the axis of rotation and θ the angle of rotation. The attitude quaternion satisfies the familiar constraint $q^T q = 1$.

From Wertz, the direction cosine matrix A transforming vectors from the navigation coordinate system to the body-fixed coordinate system is found from the quaternion using the formula

$$A(q) = (|q_4|^2 - |\mathbf{q}|^2) \mathbf{I}_{3 \times 3} + 2\mathbf{q}\mathbf{q}^T - 2q_4[\mathbf{q} \times] \quad (6.2)$$

where the cross product skew-symmetric matrix is given by

$$[\mathbf{q} \times] = \begin{bmatrix} 0 & -q_3 & q_2 \\ q_3 & 0 & -q_1 \\ -q_2 & q_1 & 0 \end{bmatrix} \quad (6.3)$$

This notation will be used in the future for any cross product matrix obtained from a 3×1 vector.

The product of two quaternions is written in the same order as the corresponding direction cosine matrices

$$A(q \otimes q') = A(q)A(q') \quad (6.4)$$

where quaternion multiplication is defined by

$$q \otimes q' = [q]q' = \begin{bmatrix} q_4 & q_3 & -q_2 & q_1 \\ -q_3 & q_4 & q_1 & q_2 \\ q_2 & -q_1 & q_4 & q_3 \\ -q_1 & -q_2 & -q_3 & q_4 \end{bmatrix} q' \quad (6.5)$$

If $\boldsymbol{\omega}$ is the angular velocity of the body with respect to the navigation frame, with components in the navigation coordinate system $\boldsymbol{\omega} = [\omega_1 \ \omega_2 \ \omega_3]^T$, the rate of change of the quaternion with respect to time is given by

$$\frac{d}{dt} q(t) = \frac{1}{2} \Omega(A\boldsymbol{\omega}(t))q(t) \quad (6.6)$$

where

$$\Omega(\boldsymbol{\omega}) = \begin{bmatrix} 0 & \omega_3 & -\omega_2 & \omega_1 \\ -\omega_3 & 0 & \omega_1 & \omega_2 \\ \omega_2 & -\omega_1 & 0 & \omega_3 \\ -\omega_1 & -\omega_2 & -\omega_3 & 0 \end{bmatrix} = \begin{bmatrix} -[\boldsymbol{\omega} \times] & \boldsymbol{\omega} \\ -\boldsymbol{\omega}^T & 0 \end{bmatrix} \quad (6.7)$$

6.2 The State Equation

The state of the spacecraft is given by the position, velocity, attitude quaternion, and two drift-rate bias vectors

$$\mathbf{x}(t) = \begin{bmatrix} \mathbf{p} \\ \mathbf{v} \\ \mathbf{b}_a \\ q \\ \mathbf{b}_g \end{bmatrix} \quad (6.8)$$

and thus has dimension 16. Here, \mathbf{p} and \mathbf{v} are understood to be in the navigation frame, while \mathbf{b}_a and \mathbf{b}_g are understood to be in the vehicle body frame. Also, q is understood to be the quaternion corresponding to the rotation from the navigation frame to the body frame. With time derivatives taken with respect to the navigation coordinate system—assumed here to be planet-fixed and rotating—the kinematic equations can be formulated as a first-order system of differential equations (Trawny et al., Meirovitch)

$$\dot{\mathbf{x}}(t) = \begin{bmatrix} \dot{\mathbf{p}} \\ \dot{\mathbf{v}} \\ \dot{\mathbf{b}}_a \\ \dot{q} \\ \dot{\mathbf{b}}_g \end{bmatrix} = \begin{bmatrix} \mathbf{v} \\ \mathbf{a} - 2[\boldsymbol{\omega}_e \times] \mathbf{v} - [\boldsymbol{\omega}_e \times]^2 \mathbf{p} \\ \mathbf{n}_{ra} \\ \frac{1}{2} \Omega(A(\boldsymbol{\omega} - \boldsymbol{\omega}_e))q \\ \mathbf{n}_{rg} \end{bmatrix} = \begin{bmatrix} \mathbf{v} \\ A^T(\mathbf{a}_m - \mathbf{b}_a - \mathbf{n}_a) + \mathbf{g} - 2[\boldsymbol{\omega}_e \times] \mathbf{v} - [\boldsymbol{\omega}_e \times]^2 \mathbf{p} \\ \mathbf{n}_{ra} \\ \frac{1}{2} \Omega(\boldsymbol{\omega}_m - \mathbf{b}_g - \mathbf{n}_g - A\boldsymbol{\omega}_e)q \\ \mathbf{n}_{rg} \end{bmatrix} \quad (6.9)$$

where $\boldsymbol{\omega}_e$ is the rotation rate of the Earth in the navigation coordinate system. The last two terms in the second row of Equation (6.9) are recognized as the Coriolis and centrifugal forces due to the rotation of the navigation frame. Note that the gyroscope senses the angular velocity of the body with respect to inertial space. Thus, to obtain the angular velocity of the body with respect to the rotating navigation frame, the rotation rate of the Earth must be subtracted from the gyro measurement. Hence the $-A\boldsymbol{\omega}_e$ term in the fourth row of Equation (6.9).

The predicted version of the state equation is obtained by taking the expectation of Equation (6.9) and using the approximation given in Equation (4.7)

$$\frac{d}{dt} \hat{\mathbf{x}}(t) = \frac{d}{dt} \begin{bmatrix} \hat{\mathbf{p}} \\ \hat{\mathbf{v}} \\ \hat{\mathbf{b}}_a \\ \hat{q} \\ \hat{\mathbf{b}}_g \end{bmatrix} = \begin{bmatrix} \hat{\mathbf{v}} \\ \hat{A}^T \hat{\mathbf{a}} + \mathbf{g} - 2[\boldsymbol{\omega}_e \times] \hat{\mathbf{v}} - [\boldsymbol{\omega}_e \times]^2 \hat{\mathbf{p}} \\ \mathbf{0} \\ \frac{1}{2} \Omega(\hat{\boldsymbol{\omega}}) \hat{q} \\ \mathbf{0} \end{bmatrix} \quad (6.10)$$

where $\hat{\mathbf{a}} = \mathbf{a}_m - \hat{\mathbf{b}}_a$, $\hat{\boldsymbol{\omega}} = \boldsymbol{\omega}_m - \hat{\mathbf{b}}_g - \hat{A}\boldsymbol{\omega}_e$, and \hat{A} is the direction cosine matrix corresponding to the predicted attitude quaternion. Propagation of the state estimate is carried out using a simple Euler method integrator.

6.3 State Error Model

Following Lefferts et al., the elements of the state error vector are given by the arithmetic difference between true and estimated quantities, as defined in Equation (4.9), with the exception of the quaternion error. Due to the constraint on the quaternion norm, a standard additive error model for the quaternion would result in a singular covariance matrix. One way to avoid this singularity is to represent P by a matrix of smaller dimension \tilde{P} . Consequently, the true quaternion is modeled as the product of the quaternion error and the estimated quaternion

$$q = \delta q \otimes \hat{q} \Leftrightarrow \delta q = q \otimes \hat{q}^{-1} \quad (6.11)$$

Since the infinitesimal attitude error corresponds to a small rotation angle, the following small angle approximation can be applied

$$\delta q \approx \begin{bmatrix} \delta \boldsymbol{\theta} \\ 1 \end{bmatrix} = \begin{bmatrix} \frac{1}{2} \delta \boldsymbol{\theta} \\ 1 \end{bmatrix} \quad (6.12)$$

and hence, the attitude error information is fully contained within the 3×1 tilt angle vector $\delta \boldsymbol{\theta}$. The uncertainty in the attitude estimate is thus characterized by a 3×3 covariance matrix of full rank.

At any time, the full 16×16 covariance matrix P can be reconstructed from the reduced 15×15 representation \tilde{P} by (Lefferts, et al.)

$$P = S\tilde{P}S^T \quad (6.13)$$

where

$$S = \begin{bmatrix} I_{9 \times 9} & O_{9 \times 3} & O_{9 \times 3} \\ O_{4 \times 9} & \Xi & O_{4 \times 3} \\ O_{3 \times 9} & O_{3 \times 3} & I_{3 \times 3} \end{bmatrix} \quad (6.14)$$

and the matrix Ξ is calculated from the attitude quaternion as

$$\Xi = \begin{bmatrix} q_4 & -q_3 & q_2 \\ q_3 & q_4 & -q_1 \\ -q_2 & q_1 & q_4 \\ -q_1 & -q_2 & -q_3 \end{bmatrix} \quad (6.15)$$

Writing the reduced-dimension state vector

$$\tilde{\mathbf{x}} = \begin{bmatrix} \mathbf{p} \\ \mathbf{v} \\ \mathbf{b}_a \\ \delta\boldsymbol{\theta} \\ \mathbf{b}_g \end{bmatrix} \quad (6.16)$$

and its corresponding predicted value (noting that the expectation value of $\delta\boldsymbol{\theta}$ is a 3×1 null vector)

$$\hat{\tilde{\mathbf{x}}} = \begin{bmatrix} \hat{\mathbf{p}} \\ \hat{\mathbf{v}} \\ \hat{\mathbf{b}}_a \\ \mathbf{0} \\ \hat{\mathbf{b}}_g \end{bmatrix} \quad (6.17)$$

the reduced-dimension state error vector is given by

$$\Delta \tilde{\mathbf{x}} = \tilde{\mathbf{x}} - \hat{\tilde{\mathbf{x}}} = \begin{bmatrix} \Delta \mathbf{p} \\ \Delta \mathbf{v} \\ \Delta \mathbf{b}_a \\ \delta \boldsymbol{\theta} \\ \Delta \mathbf{b}_g \end{bmatrix} \quad (6.18)$$

The continuous-time linearized dynamics for the state error are found using Equation (4.11), where the continuous-time state transition matrix F can be written

$$F = \begin{bmatrix} 0_{3 \times 3} & I_{3 \times 3} & 0_{3 \times 3} & 0_{3 \times 3} & 0_{3 \times 3} \\ 0_{3 \times 3} & 0_{3 \times 3} & -\hat{A}^T & -\hat{A}^T [\hat{\mathbf{a}} \times] & 0_{3 \times 3} \\ 0_{3 \times 3} & 0_{3 \times 3} & 0_{3 \times 3} & 0_{3 \times 3} & 0_{3 \times 3} \\ 0_{3 \times 3} & 0_{3 \times 3} & 0_{3 \times 3} & -[\hat{\boldsymbol{\omega}} \times] & -I_{3 \times 3} \\ 0_{3 \times 3} & 0_{3 \times 3} & 0_{3 \times 3} & 0_{3 \times 3} & 0_{3 \times 3} \end{bmatrix} \quad (6.19)$$

and the input noise sensitivity matrix G is given by

$$G = \begin{bmatrix} 0_{3 \times 3} & 0_{3 \times 3} & 0_{3 \times 3} & 0_{3 \times 3} \\ -\hat{A}^T & 0_{3 \times 3} & 0_{3 \times 3} & 0_{3 \times 3} \\ 0_{3 \times 3} & I_{3 \times 3} & 0_{3 \times 3} & 0_{3 \times 3} \\ 0_{3 \times 3} & 0_{3 \times 3} & -I_{3 \times 3} & 0_{3 \times 3} \\ 0_{3 \times 3} & 0_{3 \times 3} & 0_{3 \times 3} & I_{3 \times 3} \end{bmatrix} \quad (6.20)$$

The second line of F is derived as follows: denote by δA the direction cosine matrix corresponding to the quaternion error δq . For infinitesimal rotations, this matrix is related to the tilt angle vector by $\delta A = -[\delta \boldsymbol{\theta} \times] + I_{3 \times 3}$. From Equations (6.4) and (6.11), the true and estimated direction cosine matrices satisfy the relationship $A = \delta A \hat{A}$. Write the state equation for \mathbf{v} as

$$\begin{aligned}
\dot{\mathbf{v}} &= \mathbf{a} \\
&= A^T (\mathbf{a}_m - \mathbf{b}_a - \mathbf{n}_a) + \mathbf{g} \\
&= \hat{A}^T ([\delta\boldsymbol{\theta} \times] + I) (\mathbf{a}_m - \mathbf{b}_a - \mathbf{n}_a) + \mathbf{g} \\
&= \hat{A}^T [\delta\boldsymbol{\theta} \times] (\mathbf{a}_m - \mathbf{b}_a - \mathbf{n}_a) + \hat{A}^T (\mathbf{a}_m - \mathbf{b}_a - \mathbf{n}_a) + \mathbf{g} \\
&= -\hat{A}^T [(\mathbf{a}_m - \mathbf{b}_a - \mathbf{n}_a) \times] \delta\boldsymbol{\theta} + \hat{A}^T (\mathbf{a}_m - \mathbf{b}_a - \mathbf{n}_a) + \mathbf{g}
\end{aligned}$$

from which it follows that (again, noting that the expectation of $\delta\boldsymbol{\theta}$ is a 3×1 null vector)

$$\left. \frac{d\dot{\mathbf{v}}}{d\mathbf{b}_a} \right|_{\hat{\mathbf{x}}} = -\hat{A}^T$$

and

$$\left. \frac{d\dot{\mathbf{v}}}{d\delta\boldsymbol{\theta}} \right|_{\hat{\mathbf{x}}} = -\hat{A}^T [(\mathbf{a}_m - \hat{\mathbf{b}}_a) \times] = -\hat{A}^T [\hat{\mathbf{a}} \times]$$

The fourth line of F is derived in Lefferts et al.

6.4 Measurement Sensitivity Matrix

Assuming that the landing surface is flat and that the navigation z -axis is normal to this surface, the relationship

$$\Pi \mathbf{p} + \rho_i (\Pi A^T \mathbf{l}_i) = 0 \tag{6.21}$$

is satisfied, where \mathbf{l}_i is the unit vector comprising the direction cosines of the i -th LIDAR beam in the body-fixed coordinate system, and the projection matrix Π is given by

$$\Pi = [0 \quad 0 \quad 1] \tag{6.22}$$

From Equation (6.21)

$$\rho_i = \frac{-\Pi \mathbf{p}}{\Pi A^T \mathbf{l}_i} \tag{6.23}$$

which can be rewritten as

$$\begin{aligned}
\rho_i &= -\Pi \mathbf{p} (\Pi \mathbf{A}^T \mathbf{l}_i)^{-1} \\
&= -\Pi \mathbf{p} (\Pi \hat{\mathbf{A}}^T (I + [\delta \boldsymbol{\theta} \times]) \mathbf{l}_i)^{-1} \\
&= -\Pi \mathbf{p} (\Pi \hat{\mathbf{A}}^T \mathbf{l}_i + \Pi \hat{\mathbf{A}}^T [\delta \boldsymbol{\theta} \times] \mathbf{l}_i)^{-1} \\
&= -\Pi \mathbf{p} (\Pi \hat{\mathbf{A}}^T \mathbf{l}_i - \Pi \hat{\mathbf{A}}^T [\mathbf{l}_i \times] \delta \boldsymbol{\theta})^{-1}
\end{aligned}$$

from which it follows that

$$\left. \frac{\partial \rho_i}{\partial \mathbf{p}} \right|_{\hat{\mathbf{x}}} = \frac{-\Pi}{\Pi \hat{\mathbf{A}}^T \mathbf{l}_i} \quad (6.24)$$

and

$$\left. \frac{\partial \rho_i}{\partial \delta \boldsymbol{\theta}} \right|_{\hat{\mathbf{x}}} = -\Pi \hat{\mathbf{p}} (\Pi \hat{\mathbf{A}}^T \mathbf{l}_i)^{-2} \Pi \hat{\mathbf{A}}^T [\mathbf{l}_i \times] \quad (6.25)$$

The partial derivatives of range with respect to the other state variables are trivially zero.

Regardless of the surface topography, each range-rate measurement is simply the component of the spacecraft velocity along the respective LIDAR direction

$$\dot{\rho}_i = (\mathbf{A}^T \mathbf{l}_i) \cdot \mathbf{v} = (\mathbf{A}^T \mathbf{l}_i)^T \mathbf{v} = \mathbf{l}_i^T \mathbf{A} \mathbf{v} \quad i = 1, 2, 3 \quad (6.26)$$

Using the notation from Equation (5.6), and defining the matrix

$$\mathbf{L} = [\mathbf{l}_1 \quad \mathbf{l}_2 \quad \mathbf{l}_3] \quad (6.27)$$

Equation (6.26) is more compactly written

$$\dot{\boldsymbol{\rho}} = \mathbf{L}^T \mathbf{A} \mathbf{v} \quad (6.28)$$

which may be recast as

$$\begin{aligned}
\dot{\boldsymbol{p}} &= L^T \delta A \hat{\boldsymbol{A}} \boldsymbol{v} \\
&= L^T (I - [\delta \boldsymbol{\theta} \times]) \hat{\boldsymbol{A}} \boldsymbol{v} \\
&= L^T \hat{\boldsymbol{A}} \boldsymbol{v} + L^T [(\hat{\boldsymbol{A}} \boldsymbol{v}) \times] \delta \boldsymbol{\theta}
\end{aligned}$$

from which it follows that

$$\left. \frac{\partial \dot{\boldsymbol{p}}}{\partial \boldsymbol{v}} \right|_{\hat{\boldsymbol{x}}} = L^T \hat{\boldsymbol{A}} \quad (6.29)$$

and

$$\left. \frac{\partial \dot{\boldsymbol{p}}}{\partial \delta \boldsymbol{\theta}} \right|_{\hat{\boldsymbol{x}}} = L^T [(\hat{\boldsymbol{A}} \boldsymbol{v}) \times] \quad (6.30)$$

The partials with respect to the other state variables vanish, and the measurement sensitivity matrix H , then, is easily formed using Equations (6.24), (6.25), (6.29), and (6.30).

6.5 Update and Propagation

Using the caret operator to denote filter corrections to the corresponding predicted quantities

$$\Delta \hat{\boldsymbol{x}}_k = \begin{bmatrix} \Delta \hat{\boldsymbol{p}}_k \\ \Delta \hat{\boldsymbol{v}}_k \\ \Delta \hat{\boldsymbol{b}}_{ak} \\ \hat{\delta \boldsymbol{\theta}}_k \\ \Delta \hat{\boldsymbol{b}}_{gk} \end{bmatrix} = K_k [z - \boldsymbol{h}(\hat{\boldsymbol{x}}_k^-)] \quad (6.31)$$

the update for the quaternion is given by

$$\hat{q}_k^+ = \hat{\delta q}_k \otimes \hat{q}_k^- \quad (6.32)$$

where

$$\hat{\delta \mathbf{q}}_k = \begin{bmatrix} \frac{1}{2} \hat{\delta \boldsymbol{\theta}}_k \\ \sqrt{1 - \frac{1}{4} \hat{\delta \boldsymbol{\theta}}_k^T \hat{\delta \boldsymbol{\theta}}_k} \end{bmatrix} \quad (6.33)$$

while the update for the remaining elements of the state estimate is the usual additive correction

$$\begin{bmatrix} \hat{\mathbf{p}}_k^+ \\ \hat{\mathbf{v}}_k^+ \\ \hat{\mathbf{b}}_{ak}^+ \\ \hat{\mathbf{b}}_{gk}^+ \end{bmatrix} = \begin{bmatrix} \hat{\mathbf{p}}_k^- \\ \hat{\mathbf{v}}_k^- \\ \hat{\mathbf{b}}_{ak}^- \\ \hat{\mathbf{b}}_{gk}^- \end{bmatrix} + \begin{bmatrix} \Delta \hat{\mathbf{p}}_k \\ \Delta \hat{\mathbf{v}}_k \\ \Delta \hat{\mathbf{b}}_{ak} \\ \Delta \hat{\mathbf{b}}_{gk} \end{bmatrix} \quad (6.34)$$

Integrating Equation (4.13), the discrete-time state transition matrix at time t_k is given by

$$\Phi_k = \exp\left(\int_{t_k}^{t_{k+1}} F(t') dt'\right) \quad (6.35)$$

while the discrete-time noise covariance matrix N_k is calculated from Equation (4.16)

$$N_k = \int_{t_k}^{t_{k+1}} \Phi(t_{k+1}, t') G(t') Q G^T(t') \Phi^T(t_{k+1}, t') dt' \quad (6.36)$$

If the time between measurements is small, Equations (6.35) and (6.36) are reasonably approximated under the assumption that the integrands are constant. The state estimate and covariance are then propagated following the extended Kalman filter procedure outlined in Section 4.

To facilitate physical interpretation of the results, the attitude is presented as yaw, pitch, and roll angles rather than the four element quaternion; the corresponding partition of the covariance matrix is converted accordingly. The conversion from the quaternion to the 3-2-1, or yaw-pitch-roll, Euler angle set is given by (Wertz)

$$\text{yaw} = \tan^{-1} \left(\frac{2(q_1 q_2 + q_3 q_4)}{q_4^2 + q_1^2 - q_2^2 - q_3^2} \right) \quad (6.37)$$

$$\text{pitch} = \sin^{-1}(2(q_4 q_2 - q_1 q_3)) \quad (6.38)$$

$$\text{roll} = \tan^{-1} \left(\frac{2(q_1 q_4 + q_2 q_3)}{q_4^2 - q_1^2 - q_2^2 + q_3^2} \right) \quad (6.39)$$

The quaternion covariance P_q is converted to the Euler angle covariance P_{ypr} using the similarity transformation (Vallado)

$$P_{ypr} \approx J P_q J^T \quad (6.40)$$

where J is the Jacobian for the transformation, i.e. the matrix of all first-order partial derivatives of the Euler angle set with respect to the quaternion. The approximation sign appears in Equation (6.40) because the Euler angles are nonlinear functions of the quaternion elements.

7 Simulation Results

A simple simulation based on the final translation and touchdown phase of the Apollo lunar landings, as described in Bennett et al., was designed to study the effectiveness of the proposed Kalman filter. This terminal phase of the descent trajectory takes place close to the landing surface and involves relatively low velocities and small attitude changes.

7.1 Model

The landing surface is assumed to be flat, and the navigation z -axis is normal to this surface and directed upward. The navigation x -axis is an arbitrary direction in the plane of the landing surface; the y -axis completes the right-handed coordinate system. For simplicity, the IMU input axes were assumed to be coincident with the vehicle body coordinate frame; in addition, the rotation of the Moon was ignored, i.e. the navigation coordinate system was taken to be inertial.

Lunar gravitational acceleration is constant, $g = 1.625 \text{ m/s}^2$, and acts in the direction opposite to the navigation z -axis. The initial conditions for the simulation were taken to be: altitude = 337 m, velocity = 20.3 m/s, flight-path angle = 0° , yaw = 45° , pitch = -14° , and roll = 0° . The vehicle is subject to a constant thrust $T = 0.98g$ acting in the vehicle body z -axis and a constant angular velocity of 0.002443 rad/s about the body y -axis. Initial conditions and IMU measurements were designed such that the vehicle lands upright at touchdown (i.e. pitch = 0°) with zero horizontal velocity and vertical velocity as small as possible.

The “actual” trajectory of the lander was computed by integrating the equations of motion, Equation (6.9), with the parameters given above. Using this actual trajectory, a set of pseudo-observations was generated; Gaussian white-noise processes with standard deviations 0.1 m and 0.1 m/s were added to the range and range-rate measurements, respectively. In addition, the accelerometer output was assumed to be corrupted by Gaussian noise with standard deviation $1 \times 10^{-3} \text{ m/s}^2$, while the sensed angular velocity was corrupted by Gaussian noise with standard deviation $1 \times 10^{-6} \text{ rad/s}$. The actual

accelerometer and gyroscope biases along all three IMU input axes were set to be 0.01 m/s² and 1 deg/hr, respectively. The standard deviations of the random drift-rate ramp noise vectors were selected such that the actual biases changed “slowly” with respect to time: $1 \times 10^{-5} [1 \ 1 \ 1]^T$ m/s³ for the accelerometer and $1 \times 10^{-8} [1 \ 1 \ 1]^T$ rad/s² for the gyro. Both the IMU and LIDAR measurement data sets were generated at a rate of 10 Hz.

To test the ability of the LIDAR measurements to improve the state estimate, the initial fix was chosen to deviate from the actual initial state. Each component of the initial position estimate exceeded its corresponding actual value by 100 m, while each component of the initial velocity estimate exceeded its corresponding actual value by 5 m/s. The initial yaw estimate differed from its actual value by 3 degrees, while pitch and roll were each off by 5 degrees. The initial covariance was selected to be consistent with the initial residuals (defined to be the actual value minus the estimated value). Moreover, the state and observation noise covariance matrices were chosen to be consistent with the noise added to the IMU and LIDAR measurements. Propagation of the state estimate was carried out assuming that the gravity model was known without error.

7.2 Discussion

Using the initial conditions given above, two separate simulations were run: one with LIDAR measurements and one without. The simulation without was performed by “blowing up” the uncertainty in the LIDAR observations, i.e. the observation covariance matrix R was arbitrarily set to be the 6×6 identity matrix multiplied by 1×10^{12} . The results can be viewed in the following figures, each of which shows a state variable and

its uncertainty versus time. The left-hand column in each figure compares the actual and estimated states, while the right-hand column contains plots of the uncertainty in the state estimate versus time. Here, uncertainty is defined as the square root of the diagonal of the state covariance matrix P as computed in the Kalman filter. The figures can be divided into pairs: the first and second figures in each pair show the results from the simulations without and with LIDAR measurements, respectively.

Figure 7.1 shows that, with no LIDAR measurements to update the state estimate, the error in position is on the order of several hundred meters and only worsens over time because of the error in velocity. However, when LIDAR measurements are introduced in the simulation (see Figure 7.2), the estimate of altitude is rapidly improved: error in z is on the order of 1 cm. Assuming a flat landing surface, the range observations have no dependence on the horizontal components of position, and thus the errors in these two estimates are propagated throughout the trajectory (note the scale of the uncertainty plots in Figure 7.2). Here, the error in lateral position is nearly constant because, with LIDAR measurements, the estimated horizontal velocities closely match the corresponding actual values.

Comparing Figures 7.3 and 7.4, the LIDAR line-of-sight velocity observations yield accurate updates on all three components of velocity. Without LIDAR measurements, error in velocity is on the order of 10 m/s and generally worsens over time due to the uncertainty in the initial estimate of velocity, accel bias, and attitude. Conversely, error in velocity is on the order of 1cm/s when LIDAR measurements are used. Note that the LIDAR geometry is most favorable for calculating the z -component of

velocity in the case of level, or near-level, flight; consequently, this part of the velocity estimate is particularly well-determined when LIDAR measurements are used.

The IMU biases are plotted in Figures 7.5 through 7.8. Here, the numerals 1, 2, and 3 denote the roll, pitch, and yaw axes of the body, respectively. Without LIDAR observations, the biases are not updated, as expected—carefully note the scales of the uncertainty plots in Figures 7.5 and 7.7. On the other hand, with LIDAR observations, the estimates of the accelerometer bias in all three directions are especially accurate (errors on the order of 10^{-4} m/s²), while the gyro biases along the roll and pitch axes are reasonably close to their actual values (errors on the order of 0.1 deg/hr). Because the LIDAR geometry is most favorable for estimating the component of velocity along the body z -axis, the accel bias estimate in this direction has the smallest uncertainty of the three. The estimate of the gyro bias along the yaw axis is quite poor, which is to be expected since the LIDAR measurements do not update the yaw angle of the vehicle in the case of a flat landing surface.

Attitude, shown in Figures 7.9 and 7.10, is poorly determined without LIDAR observations because of the uncertainty in the initial estimate and because the gyro bias is unknown. In this case, attitude errors are on the order of several degrees. While there is no improvement in the yaw estimate (again, to be expected), the estimates of pitch and roll are quite accurate in the case when LIDAR measurements are used: errors are on the order of 0.01 deg.

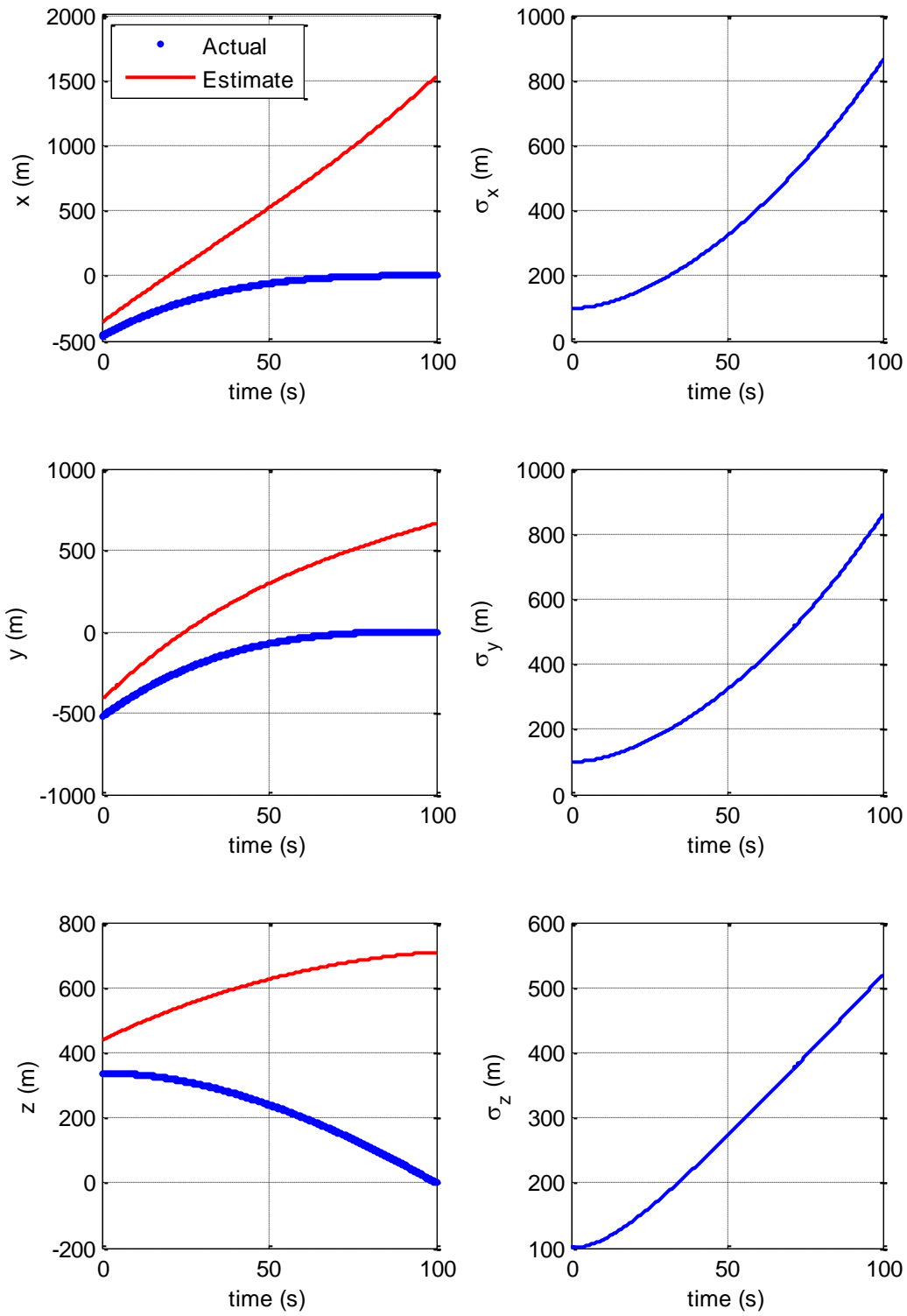


Figure 7.1: History of position estimate and uncertainty without LIDAR.

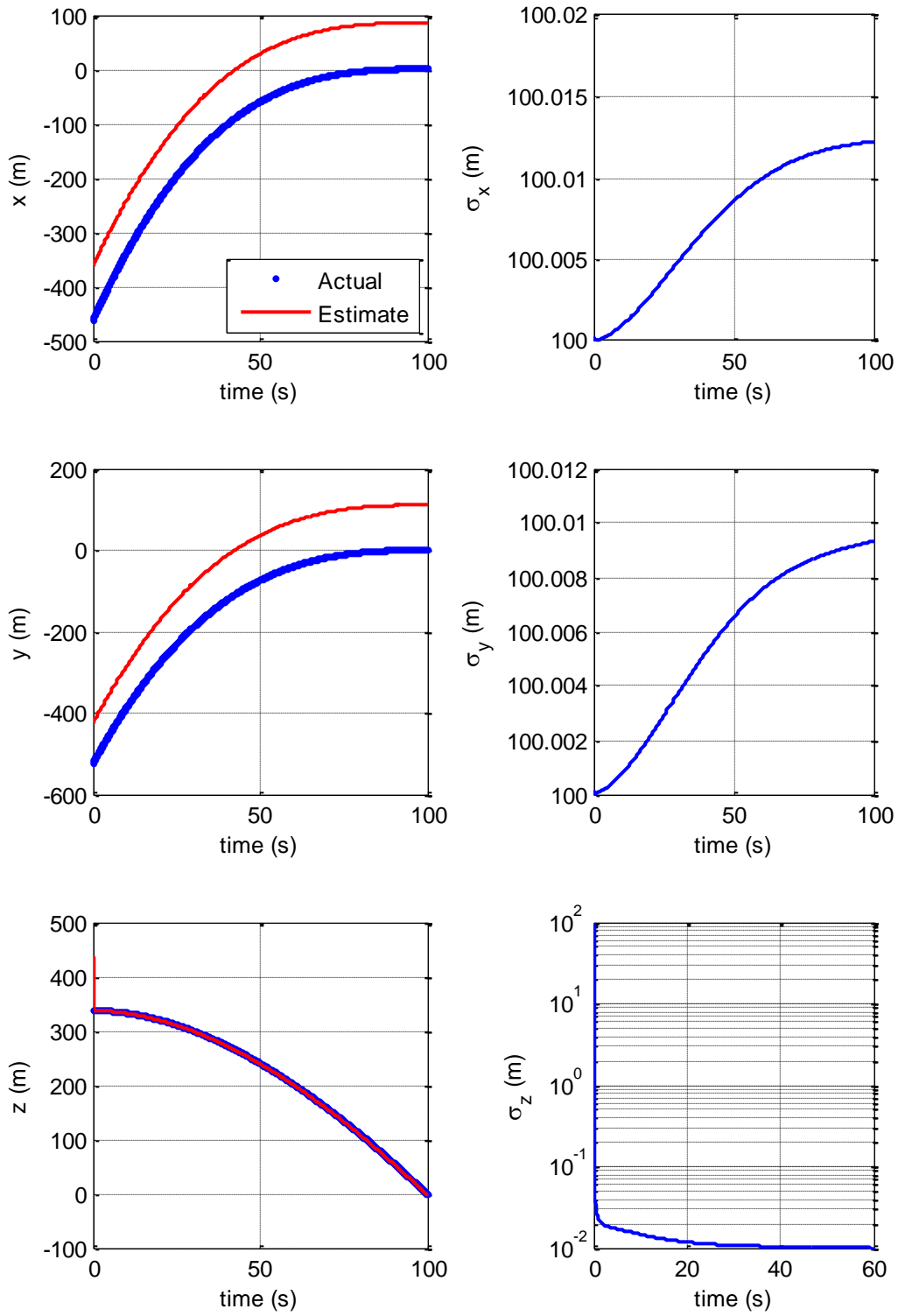


Figure 7.2: History of position estimate and uncertainty with LIDAR.

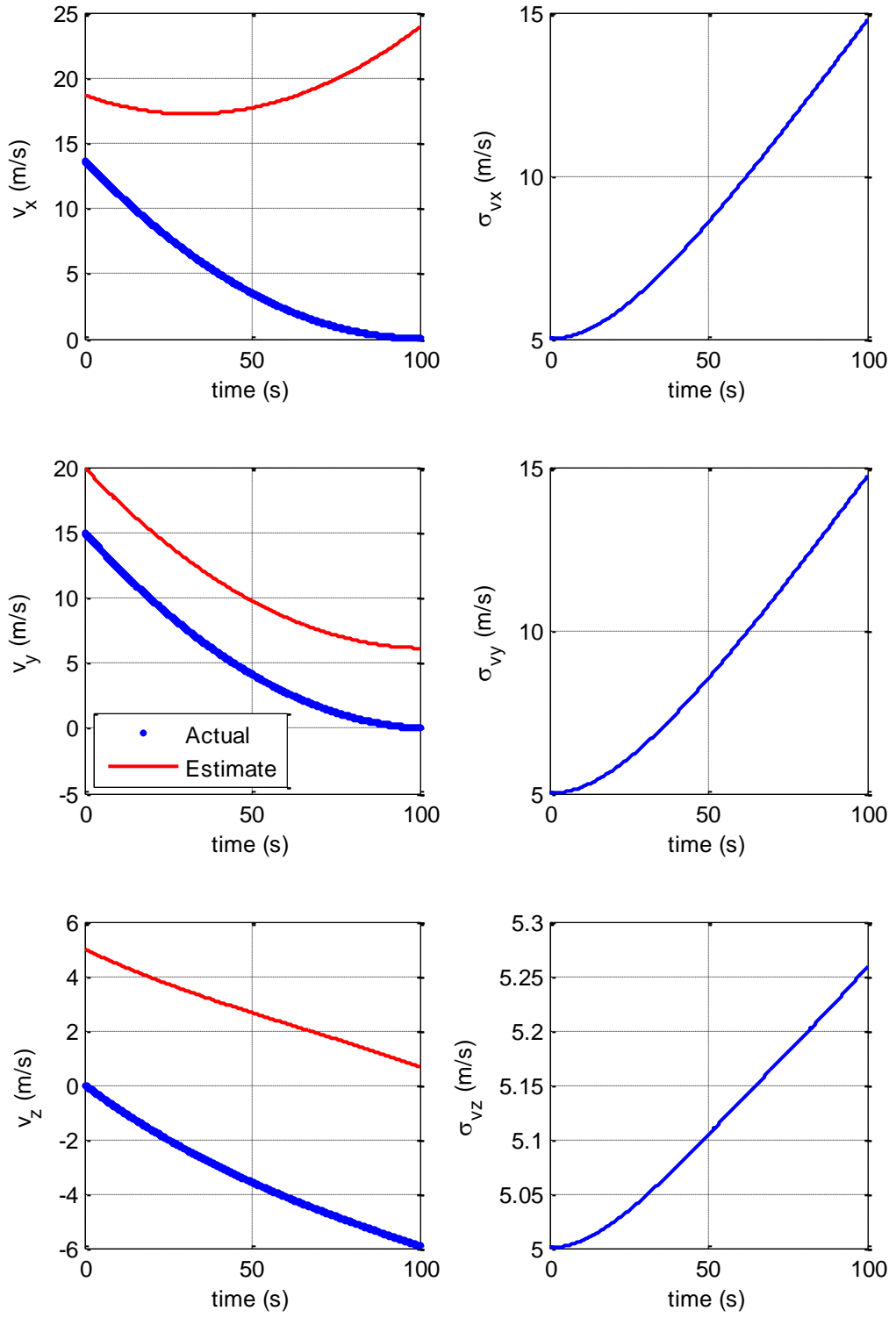


Figure 7.3: History of velocity estimate and uncertainty without LIDAR.

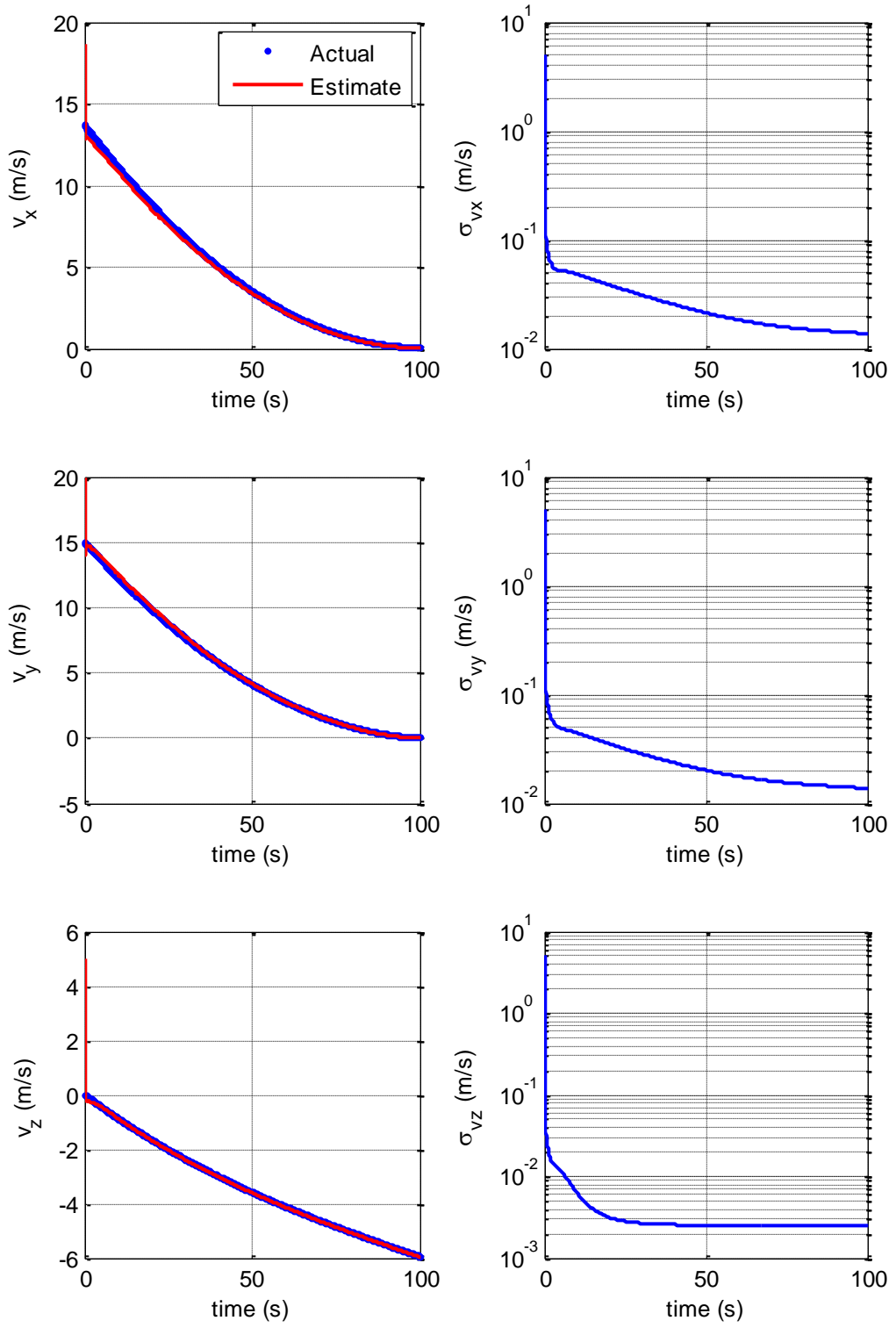


Figure 7.4: History of velocity estimate and uncertainty with LIDAR.

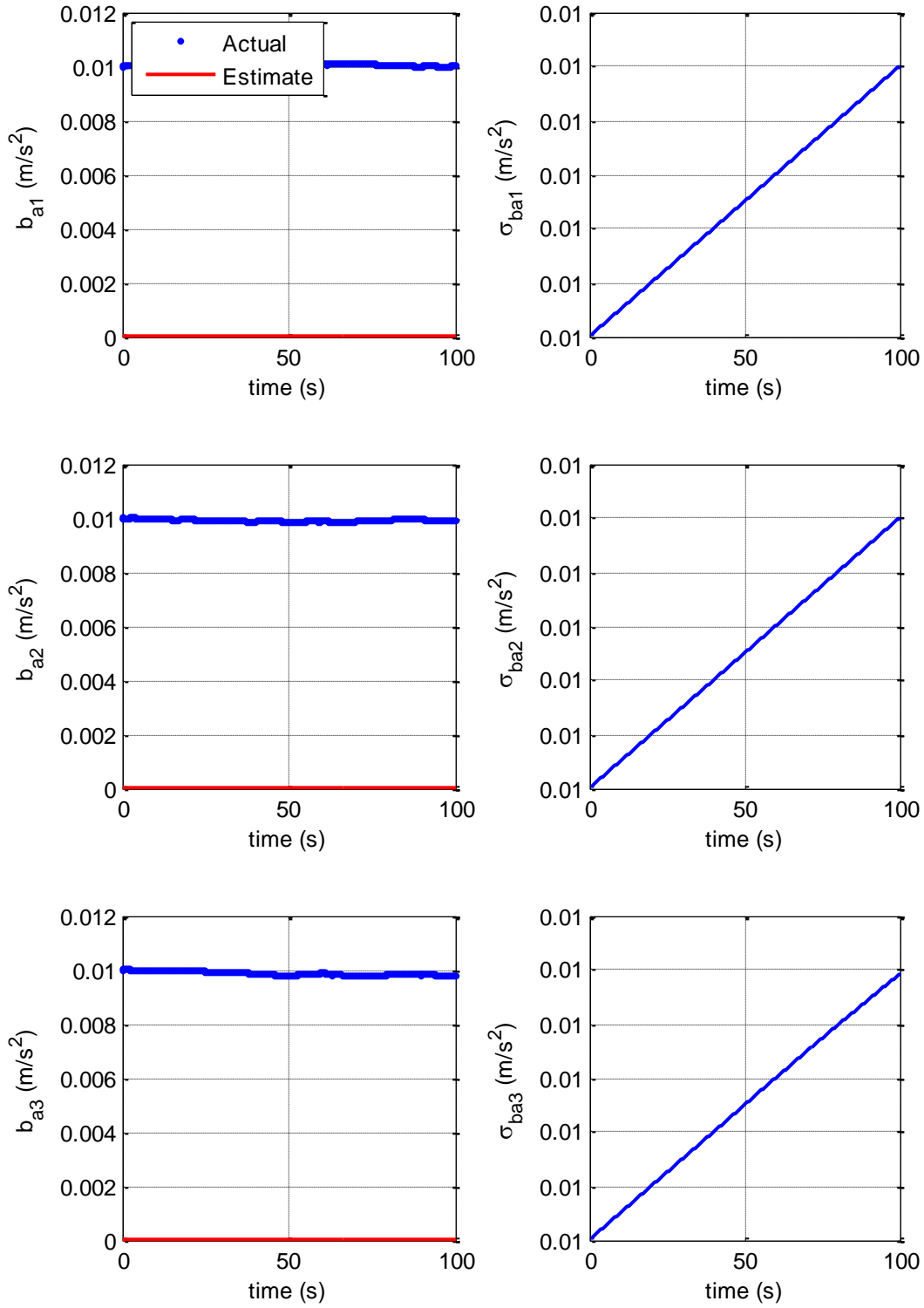


Figure 7.5: History of accel bias estimate and uncertainty without LIDAR.

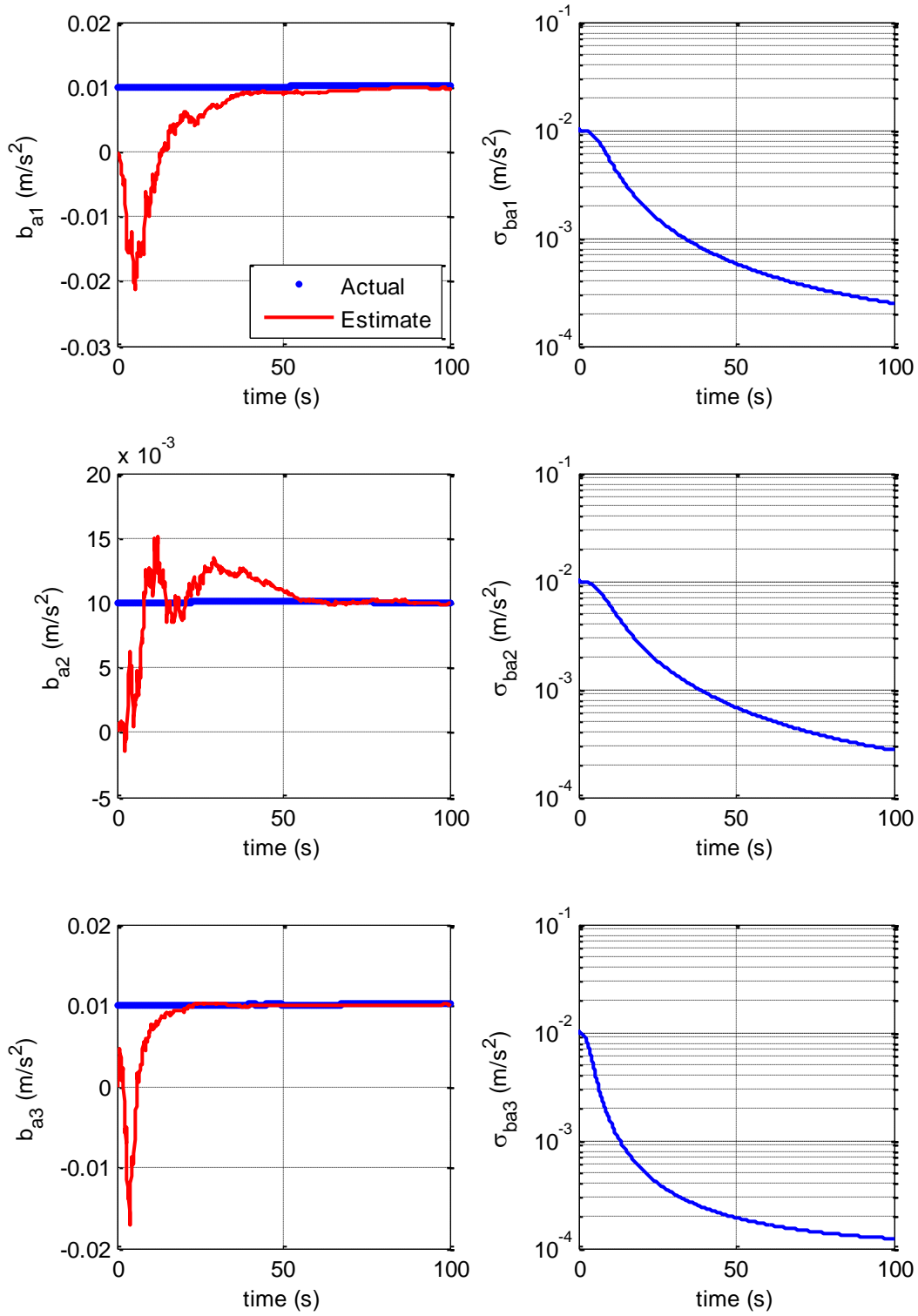


Figure 7.6: History of accel bias estimate and uncertainty with LIDAR.

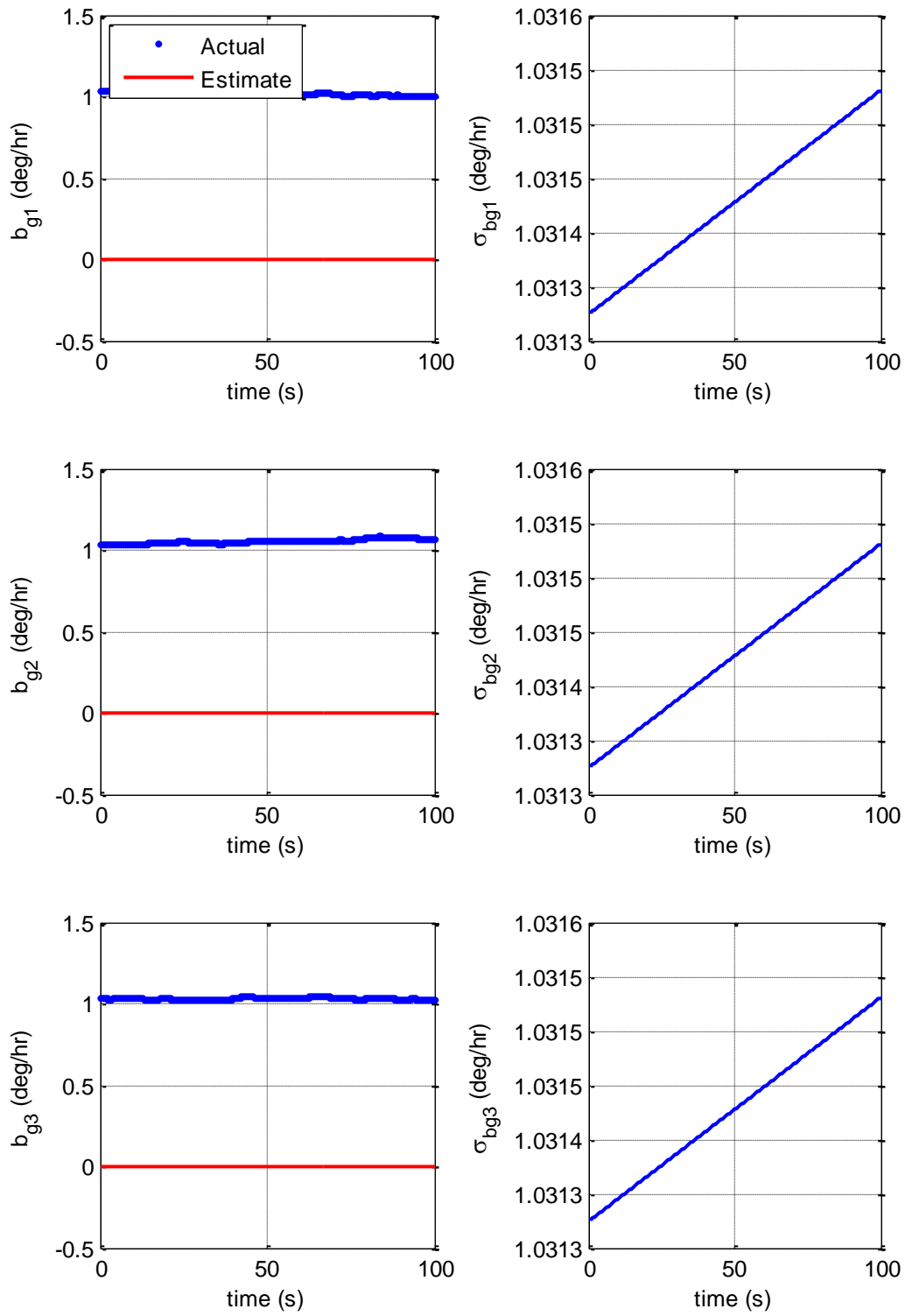


Figure 7.7: History of gyro bias estimate and uncertainty without LIDAR.

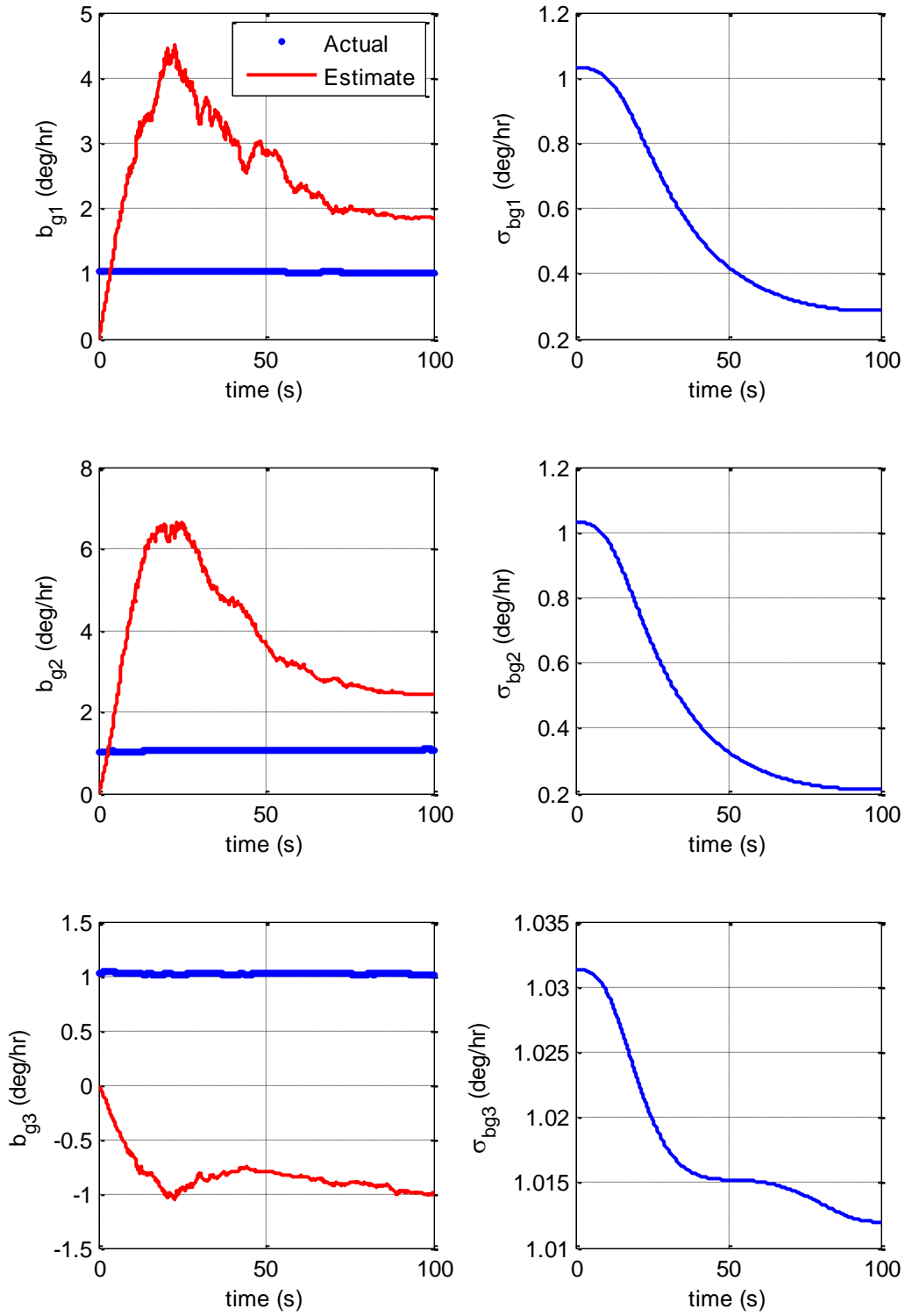


Figure 7.8: History of gyro bias estimate and uncertainty with LIDAR.

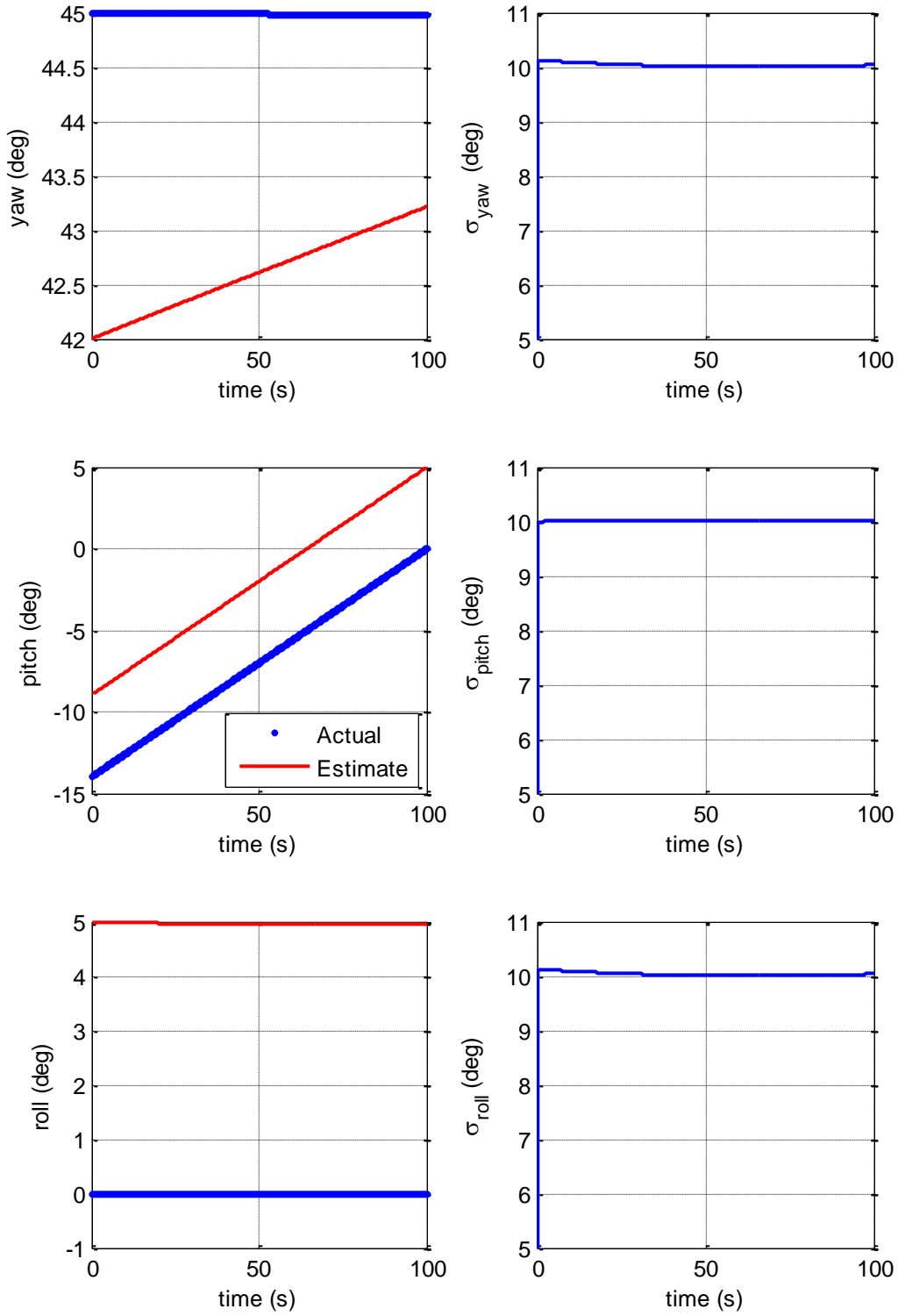


Figure 7.9: History of attitude estimate and uncertainty without LIDAR.

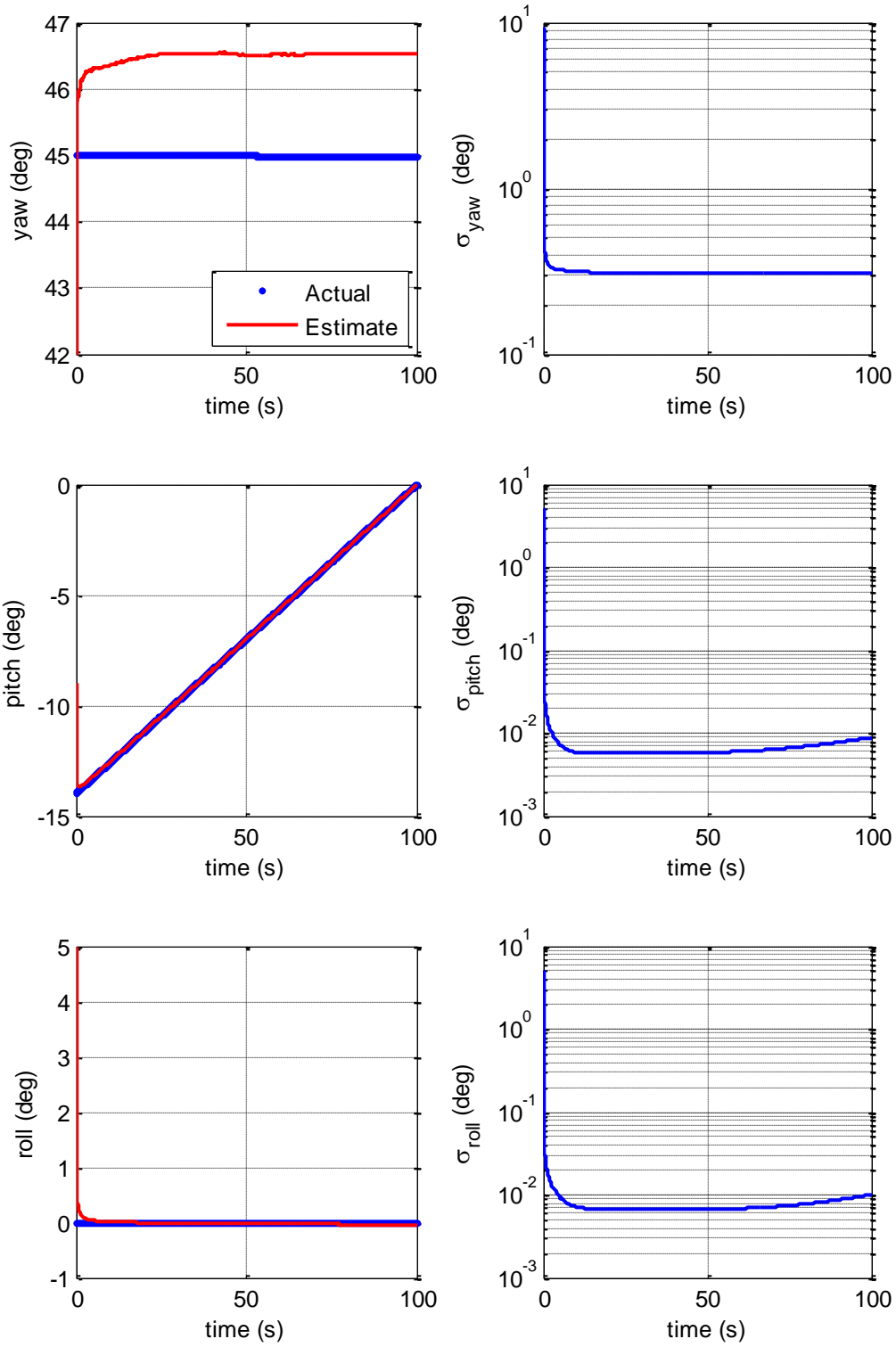


Figure 7.10: History of attitude estimate and uncertainty with LIDAR.

8 Experimental Results

A LIDAR system developed at NASA Langley Research Center was installed aboard a Eurocopter AS350D helicopter and tested in a series of six flights over the California desert near NASA Dryden from August 20-22, 2008. This section presents the results from analysis of the second flight test, which occurred over a flat, dry lake bed.

8.1 Model

The LIDAR was mounted on the nose of the helicopter inside a gimbaled spherical shroud, which was designed to point nadir throughout the flight. Unfortunately, due to problems with the gimbal control software, nadir-lock was not maintained when the helicopter turned. LIDAR measurements of range and range-rate, as provided by Diego Pierrottet of Coherent Applications, Inc., were taken at the rate of 10 Hz. The helicopter was also equipped with an onboard GPS sensor. Although there is obviously error in any observation, uncertainties in GPS measurements (on the order of 1 cm and 1 cm/s for position and velocity, respectively) are small enough to justify taking GPS-measured position and velocity to represent the “actual” state of the helicopter.



Figure 8.1: Flight test helicopter

In addition, a Northrop Grumman LN-200 Inertial Measurement Unit was mounted along with the LIDAR inside of the shroud at the front of the helicopter. IMU measurements were sampled at the rate of 400 Hz. According to the LN-200 specifications, the accelerometer bias is 0.003 to 0.03 m/s^2 , while the gyro bias is between 1 and 10 deg/hr. The IMU x -, y -, and z -axes do not correspond to the respective axes in the body frame; the transformation mapping the measured acceleration and angular velocity vectors in the IMU frame to the body frame is given by

$$R_i^b = \begin{bmatrix} 0 & 1 & 0 \\ 0 & 0 & 1 \\ 1 & 0 & 0 \end{bmatrix} \quad (8.1)$$

Raw IMU data—supplied by Jason Keim of the Guidance and Control Analysis Group at Jet Propulsion Laboratory (JPL)—is presented as incremental changes in velocity and angles versus time. Numerical derivatives (i.e. acceleration and angular rates), as required for evaluation of the equations of motion, were calculated using a first-order forward-difference approximation scheme.

Including only the central term in the gravity model, the gravity vector can be written in the LGCV frame

$$\mathbf{g}^c = -\frac{GM}{p^2} \begin{bmatrix} 0 \\ 0 \\ 1 \end{bmatrix} \quad (8.2)$$

With the rotation given in Equation (3.1), the gravity vector is represented in the LGV frame as

$$\mathbf{g}^v = R_c^v \mathbf{g}^c = -\frac{GM}{p^3} \begin{bmatrix} p_x \\ 0 \\ p_z \end{bmatrix} \quad (8.3)$$

Using GPS measurements of the helicopter position, also provided by Jason Keim, the gravity vector in the LGV frame at the initial position of the helicopter was found to be

$$\mathbf{g}^v = \begin{bmatrix} 0.030928 \\ 0 \\ -9.81745 \end{bmatrix} \text{m/s}^2 \quad (8.4)$$

For simplicity, gravity was held at this constant value throughout the navigation sequence since variation in the helicopter's position was no more than a few kilometers, which is insignificant compared to the 6378 km radius of the Earth. Local gravity anomalies and gravitational perturbations due to the oblateness of the Earth were ignored.

The angular velocity of the Earth is expressed in the ECEF frame as

$$\boldsymbol{\omega}_e^e = \omega_e \begin{bmatrix} 0 \\ 0 \\ 1 \end{bmatrix} \quad (8.5)$$

Using the direction cosine matrix given in Equation (3.2), the angular velocity of the Earth is written in the LGV frame

$$\boldsymbol{\omega}_e^v = R_e^v \boldsymbol{\omega}_e^e = \omega_e \begin{bmatrix} \cos \varphi \\ 0 \\ \sin \varphi \end{bmatrix} \quad (8.6)$$

At the initial latitude of the helicopter, the angular velocity vector was found to be

$$\boldsymbol{\omega}_e^v = \begin{bmatrix} 5.976209 \\ 0 \\ 4.178500 \end{bmatrix} \times 10^{-5} \text{ rad/s} \quad (8.7)$$

To simplify the Kalman filter calculations, a modified version of the LGV frame was used as the navigation coordinate system. The origin of the navigation frame was arbitrarily selected to be the point on the surface directly below the initial position of the helicopter, as measured along the local geodetic vertical. The z -axis is coincident with the local geodetic vertical at this point; the x - and y -axes are directed toward geodetic north and west, respectively. Here, it should be noted that GPS provides altitude measurements relative to mean sea level, but LIDAR measures distance to the local surface, which was

assumed to be flat. Consequently, the elevation of the test site had to be determined using a value that yielded a best fit of the two data sets, namely 665 m. In addition, unlike the conventional LGV system, the navigation frame does not rotate with vehicle position but is fixed with respect to the Earth. Since the system is planet-fixed, it rotates with the angular velocity given in Equation (8.7).

8.2 Discussion

Figure 8.2 shows the ground track of the vehicle, as measured by the GPS, for the time period during which LIDAR observations were available. The red circle in the figure denotes the initial position, while the red cross indicates the final position. It can be seen that the helicopter performed a series of figure eight maneuvers, alternately flying with northeast and southwest headings. Figure 8.3 is a plot of altitude above the surface versus time; the helicopter flew fairly level at the beginning of the flight and performed a steep ascent and dive at the end. Total flight time was roughly one half-hour.

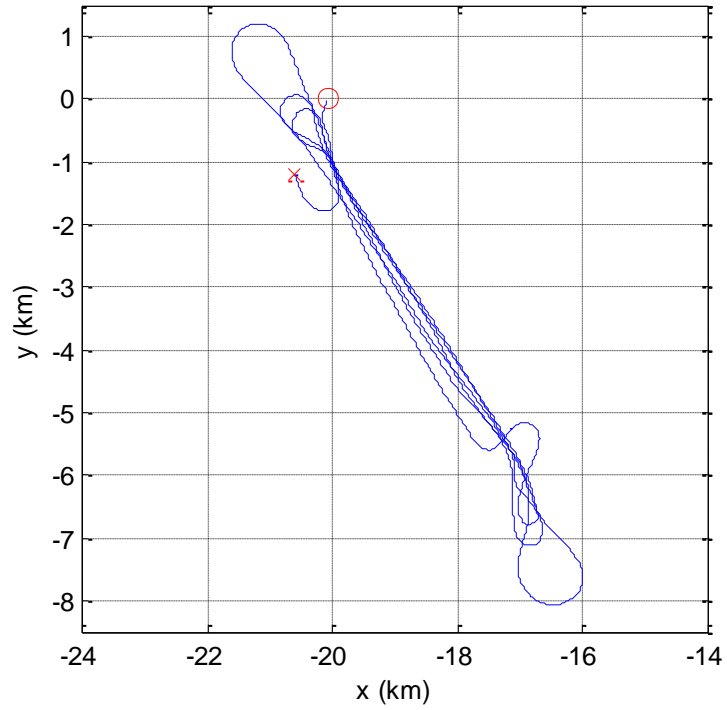


Figure 8.2: Ground track of helicopter as measured by GPS.

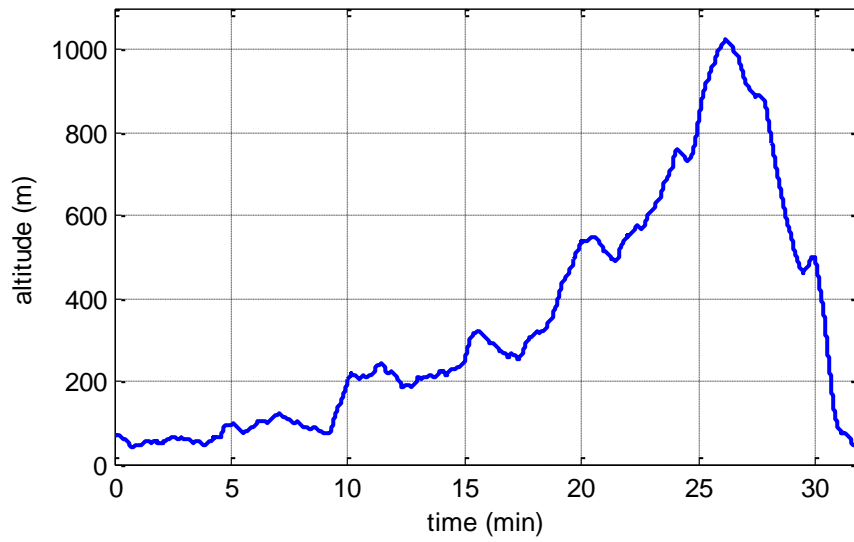


Figure 8.3: Altitude above surface versus time as measured by GPS.

Unfortunately, due to problems with the signal processing algorithm and limitations of the hardware components in the LIDAR breadboard system, much of the range and range-rate data was corrupted by significant noise and therefore unusable. However, it was possible to study a 2.5 minute interval near the beginning of the flight, which was the time period with the most viable data. As in Section 7, the Kalman filter routine was run with and without LIDAR measurements to estimate the state of the helicopter over time. In both cases, initial estimates for position, velocity, and attitude were set equal to the corresponding “actual” initial conditions. (Quotations are used here since the true state of the vehicle is unknowable. GPS measurements are taken to represent the “actual” position and velocity; “actual” attitude is taken to be the yaw-pitch-roll provided by JPL.) Initial estimates for the accelerometer and gyro biases were set to zero along all three body axes.

The Kalman filter was tuned by trial and error to minimize the residuals, defined as the difference between the actual and estimated values. Results are shown in the figures that follow, which have a format similar to those in Section 7. Residuals are plotted in the right-hand column in the position, velocity, and attitude figures. Estimated uncertainties are plotted in the accelerometer and gyro bias figures since the actual biases are unknown.

As shown in Section 7, the estimate of the accelerometer bias cannot be improved without LIDAR observations. Because the bias changes very slowly in time, the error in this parameter is nearly constant. Likewise, error in the gravity model is also nearly constant since gravitational acceleration cannot be expected to vary significantly from

one time or location to the next. The combination of these constant errors in acceleration yields linear errors in velocity and quadratic errors in position, which can be seen in Figures 8.4 and 8.6. This is not true for the y -component, though, possibly because the two errors in this direction partially cancel one another.

LIDAR observations, however, mitigate much of the error associated with the uncertainties in the gravity model and accelerometer bias. As seen in Figure 8.5, by the end of the 2.5 minute period, the LIDAR has reduced the error in the x -component of position by an order of magnitude when compared to the IMU-only case. Error in altitude is two orders of magnitude less than that in the case of exclusive IMU integration. Range-rate measurements update all three components of the velocity vector, which has the effect of improving the position estimates. The estimate in z is best, however, since range measurements only update this component of position in the case of a flat surface. Also, as previously noted, the LIDAR geometry is most favorable for estimating the z -component of velocity for level flight.

The effect of the LIDAR observations on the velocity estimate is shown in Figure 8.7. Residuals in this case are on the order of 0.1 m/s, an order of magnitude less than the residuals at the 200 s mark without the LIDAR.

Figures 8.8 through 8.11 contain plots of the bias estimates with and without LIDAR observations. As mentioned previously, the biases are not updated in the case without the LIDAR (carefully note the scales in Figures 8.8 and 8.10). With the LIDAR, the accelerometer bias estimates (the best of which is along the vehicle yaw axis, as in the simulation) are on the order of 0.01 m/s^2 , within the bounds listed in the IMU

specifications. Gyro bias estimates are on the order of 0.1 deg/hr, which is less than the bias listed in the IMU specifications but not unreasonable. As in the simulation, the gyro bias along the vehicle yaw axis is not well-determined. The “jumpiness” in the other two gyro estimates is likely due to the inability of the LIDAR to accurately determine the attitude of the helicopter.

Here, it should be noted that because gravity and specific force appear as part of an algebraic sum in the equations of motion, errors in these two terms are indistinguishable to the Kalman filter. Accordingly, the part of the measurement residual which is actually due to the gravity model error is mistakenly assigned by the filter to accelerometer bias. This phenomenon is known as aliasing. The simple gravity model used here certainly differs from the actual gravity field, and thus the gravity model error has been aliased into the estimated accelerometer bias.

Because the gyro bias is nearly constant, errors in the Euler angles should be linearly increasing in the case of IMU-only integration. For the short 2.5 minute period under investigation, the attitude estimates without LIDAR are quite good since the gyro bias is so small. Over long time periods, however, even slight gyro drift would cause substantial attitude errors. Assuming a flat surface, the LIDAR measurements only update the pitch and roll estimates; residuals for these two angles are on the order of 0.1 deg. Yaw is not updated, as expected. The LIDAR measurements prevent the pitch and roll estimates from drifting but also introduce fairly significant noise, possibly due to local terrain undulations or misalignment of the LIDAR beams.

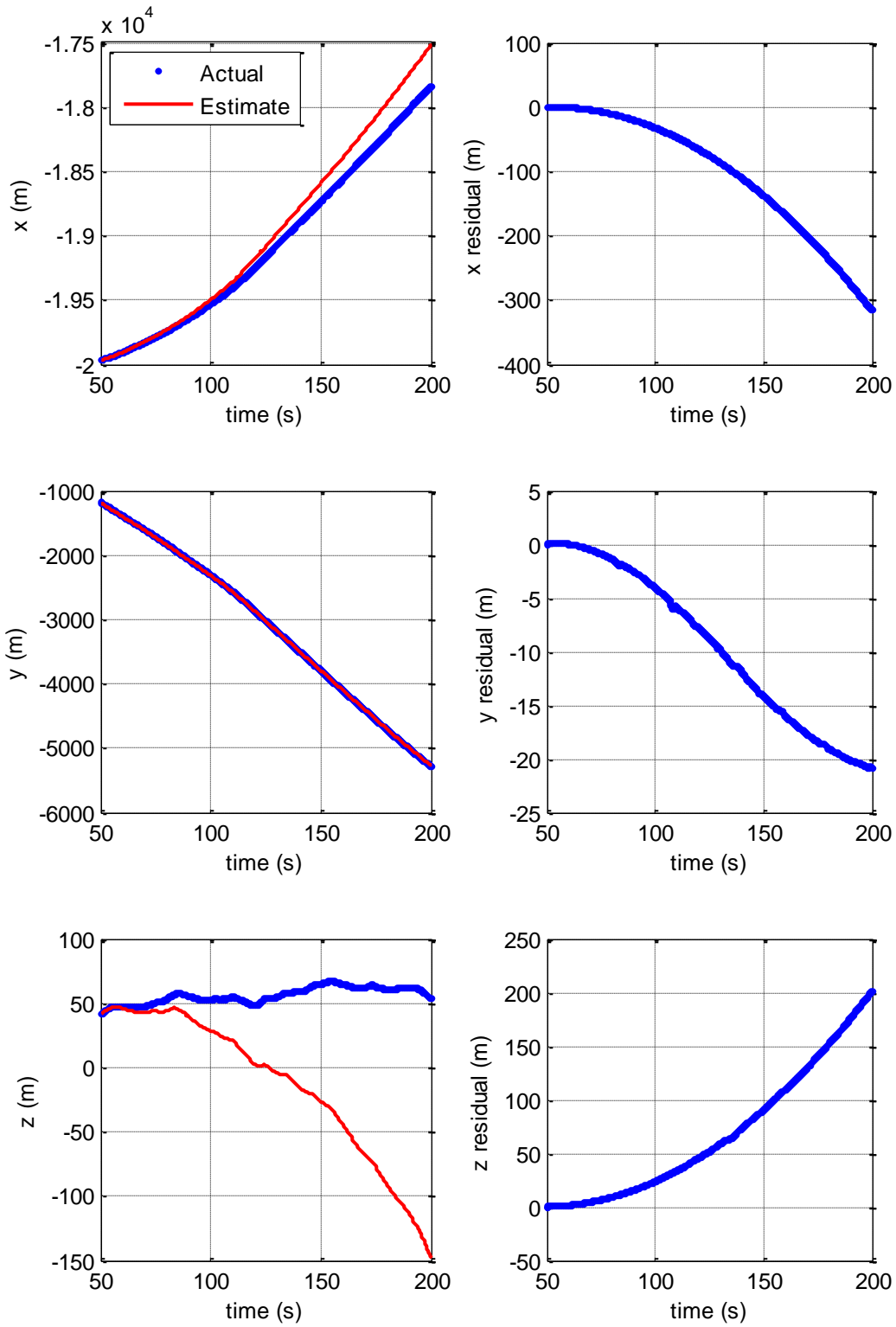


Figure 8.4: Position estimate and residual versus time without LIDAR.

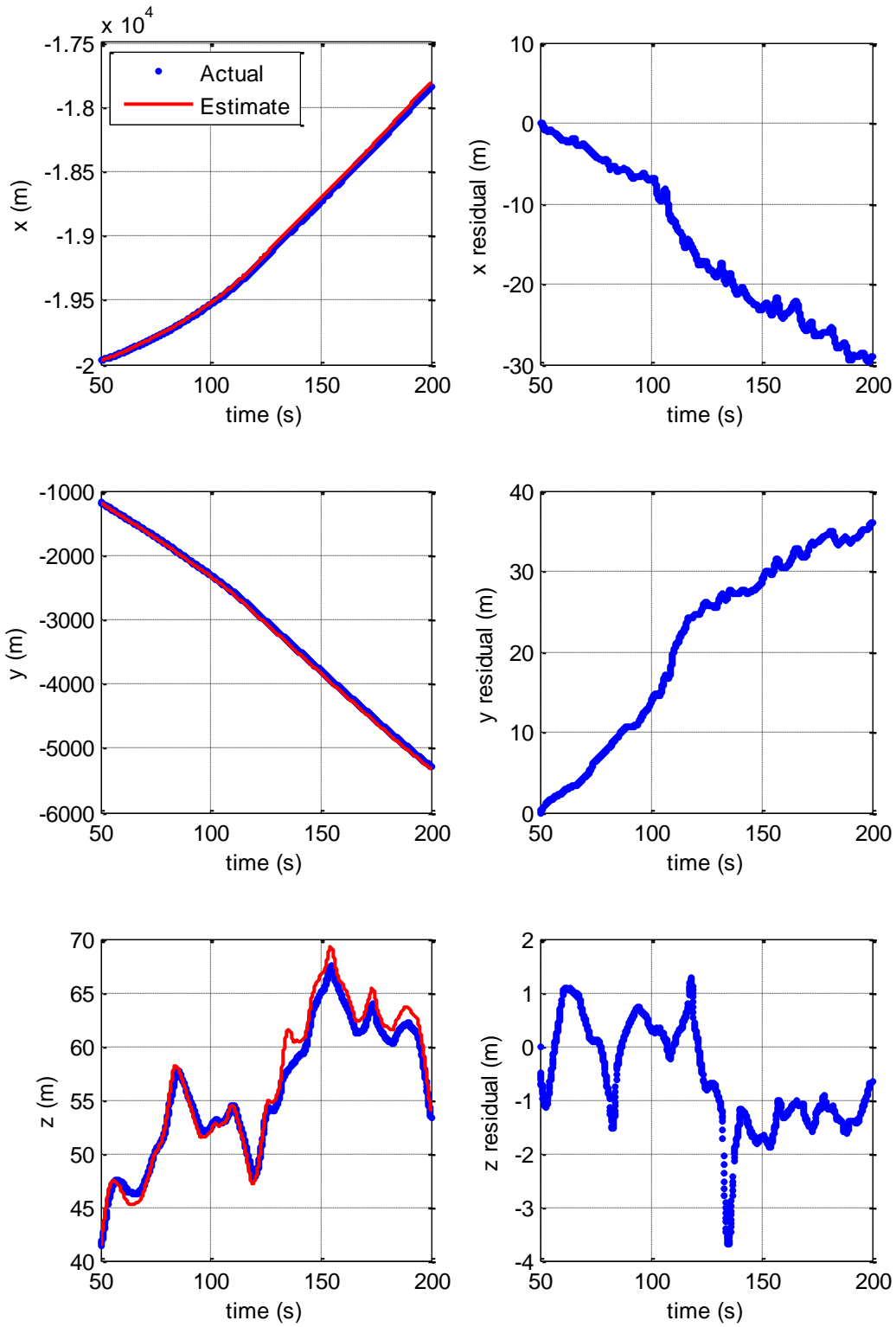


Figure 8.5: Position estimate and residual versus time with LIDAR.

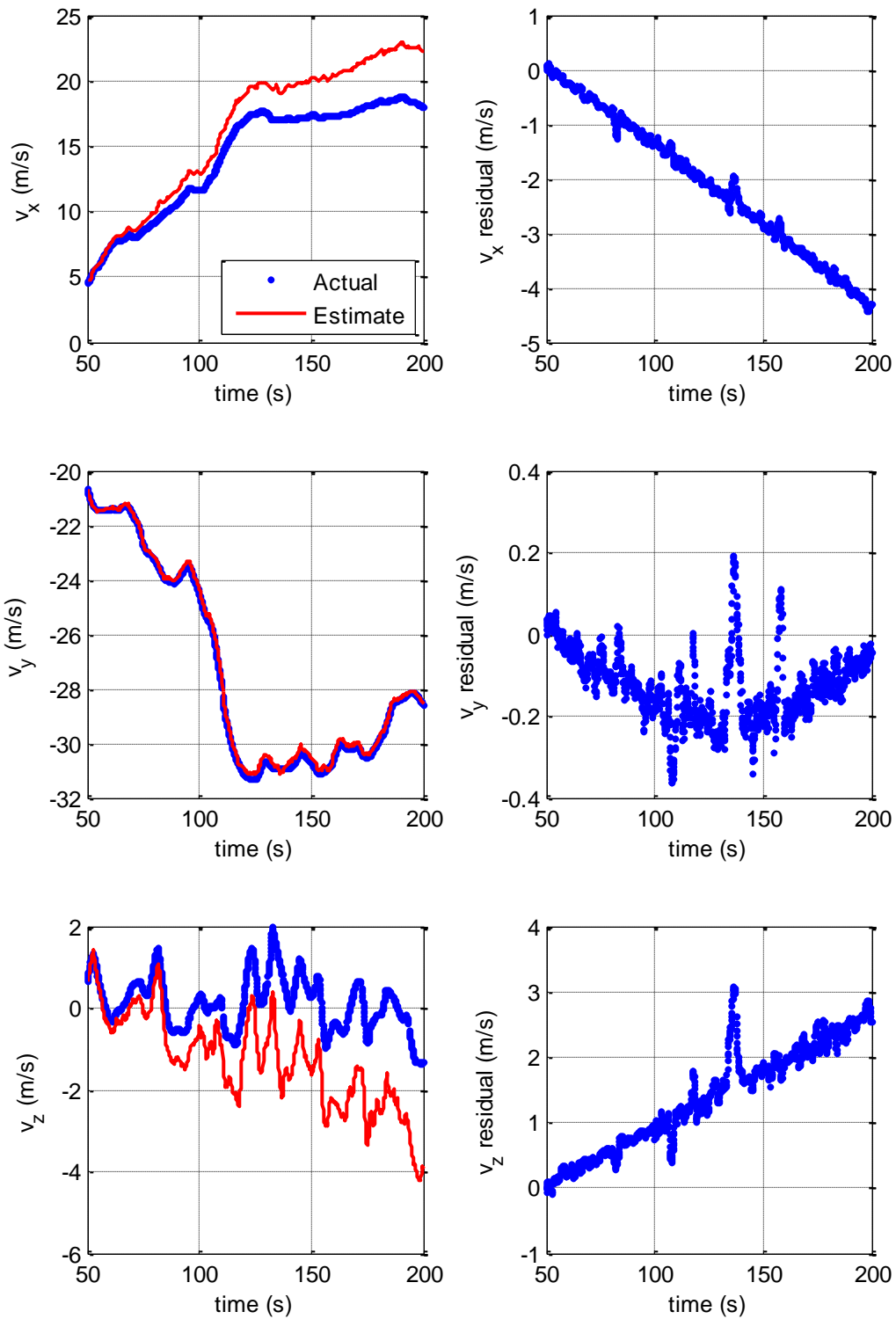


Figure 8.6: Velocity estimate and residual versus time without LIDAR.

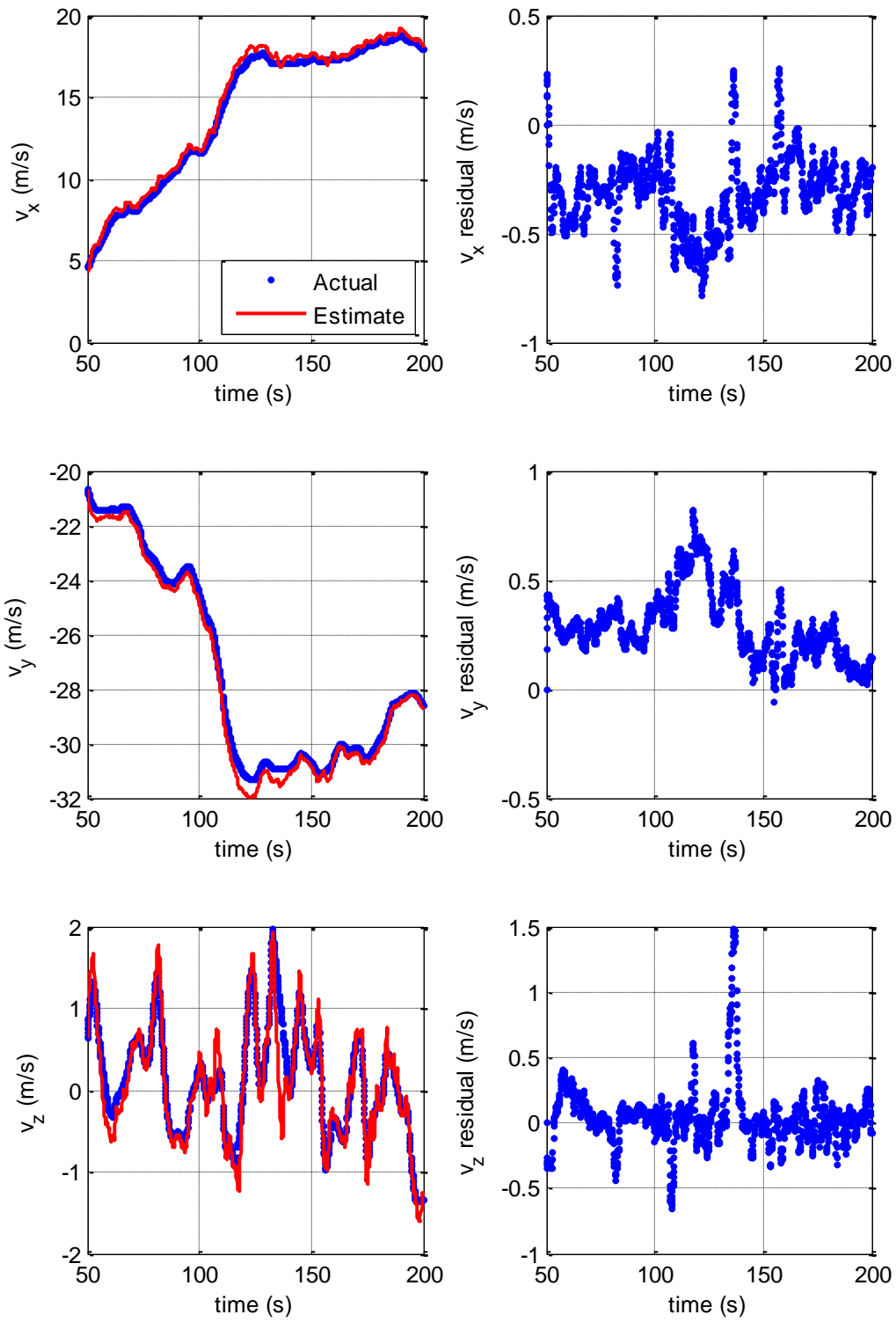


Figure 8.7: Velocity estimate and residual versus time with LIDAR.

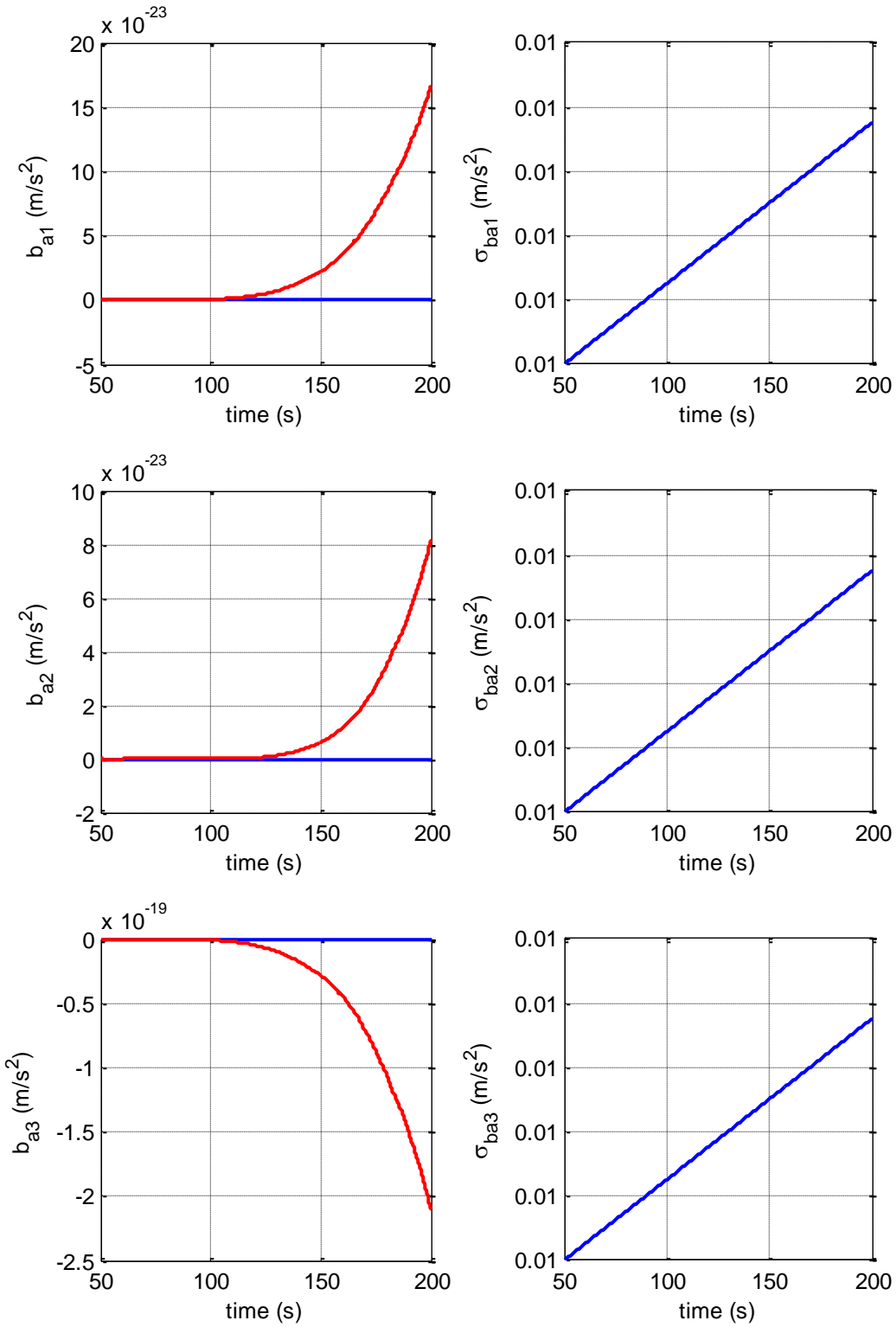


Figure 8.8: Accelerometer bias estimate and uncertainty versus time without LIDAR.

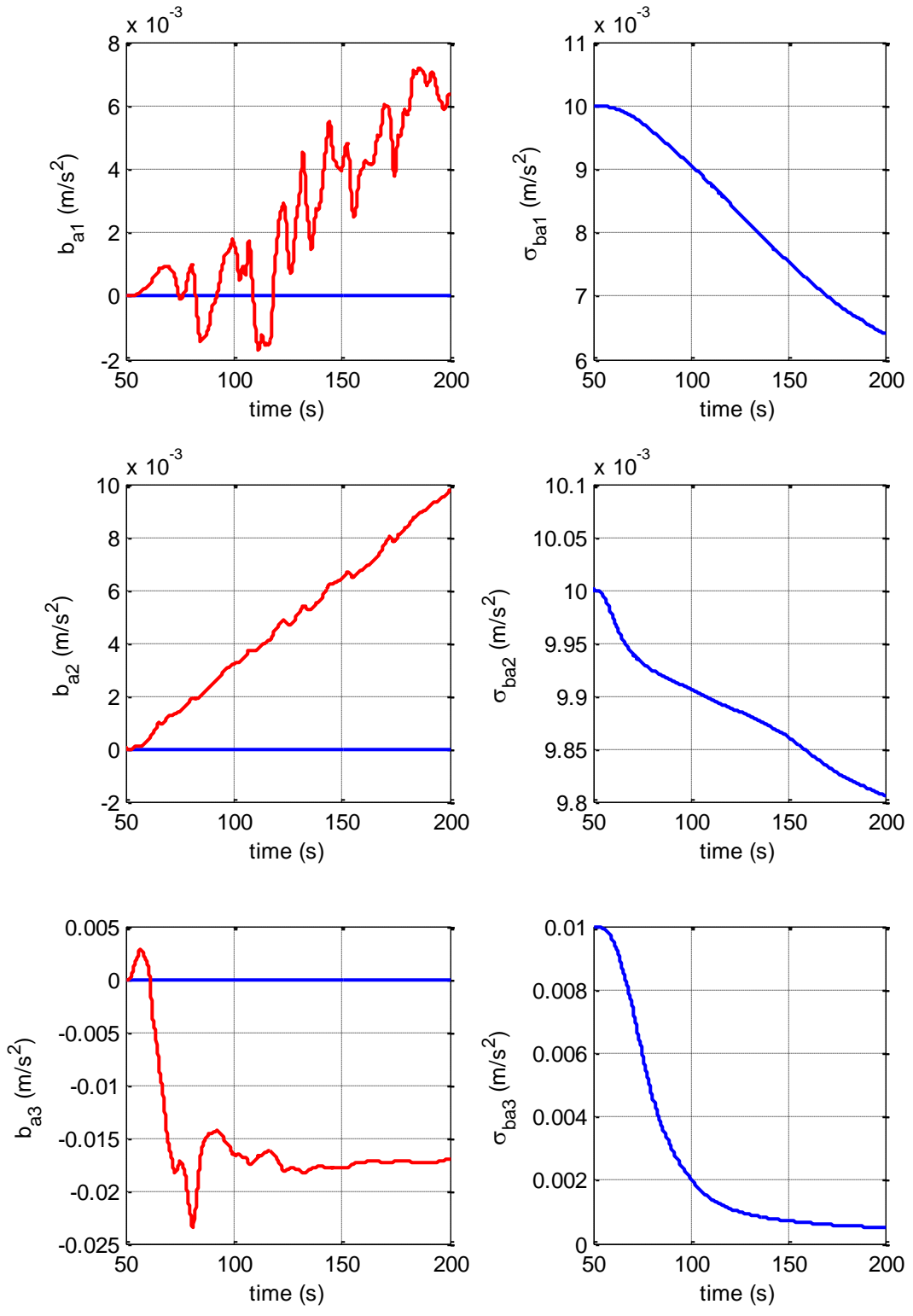


Figure 8.9: Accelerometer bias estimate and uncertainty versus time with LIDAR.

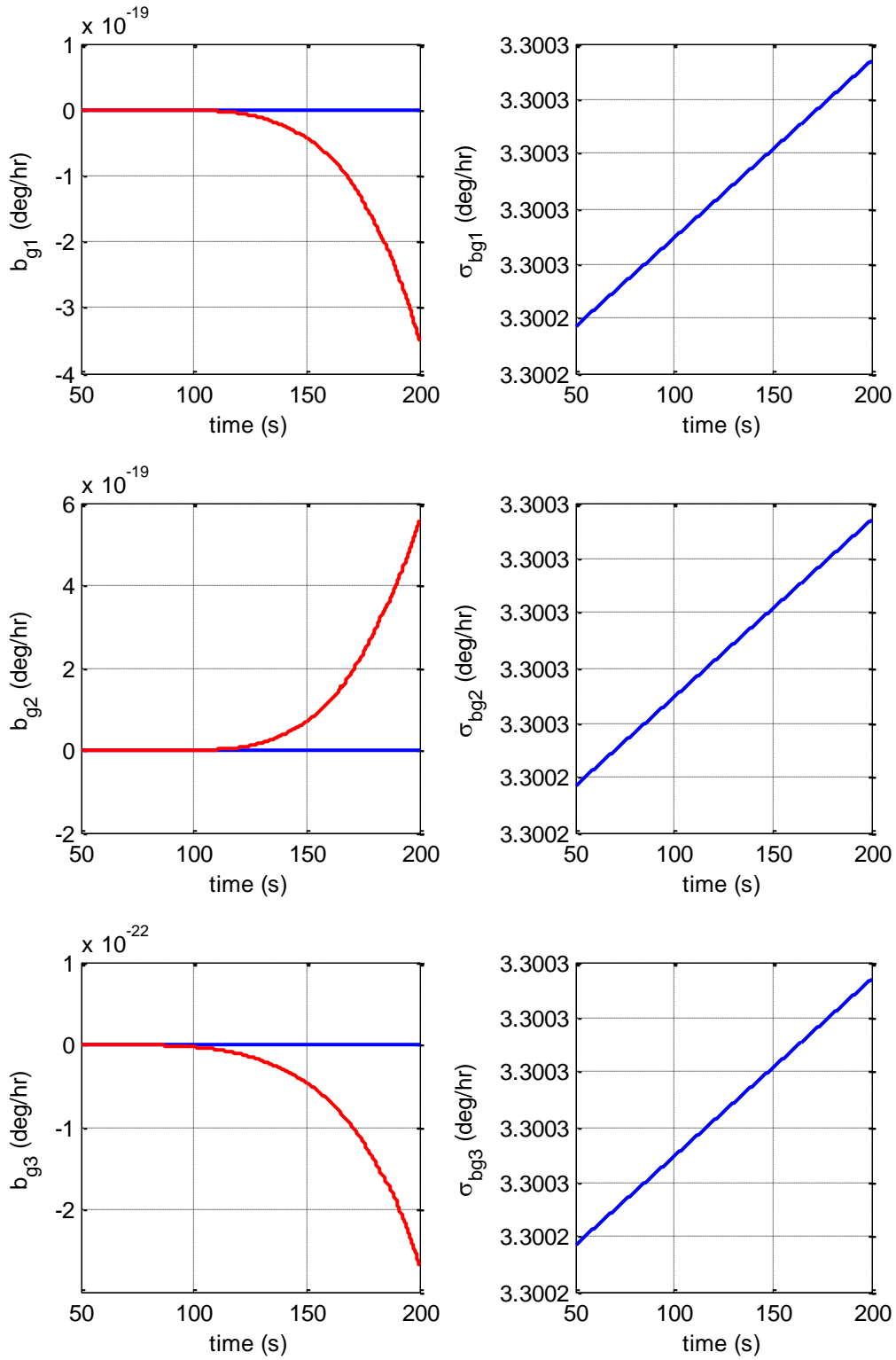


Figure 8.10: Gyro bias estimate and uncertainty time without LIDAR.

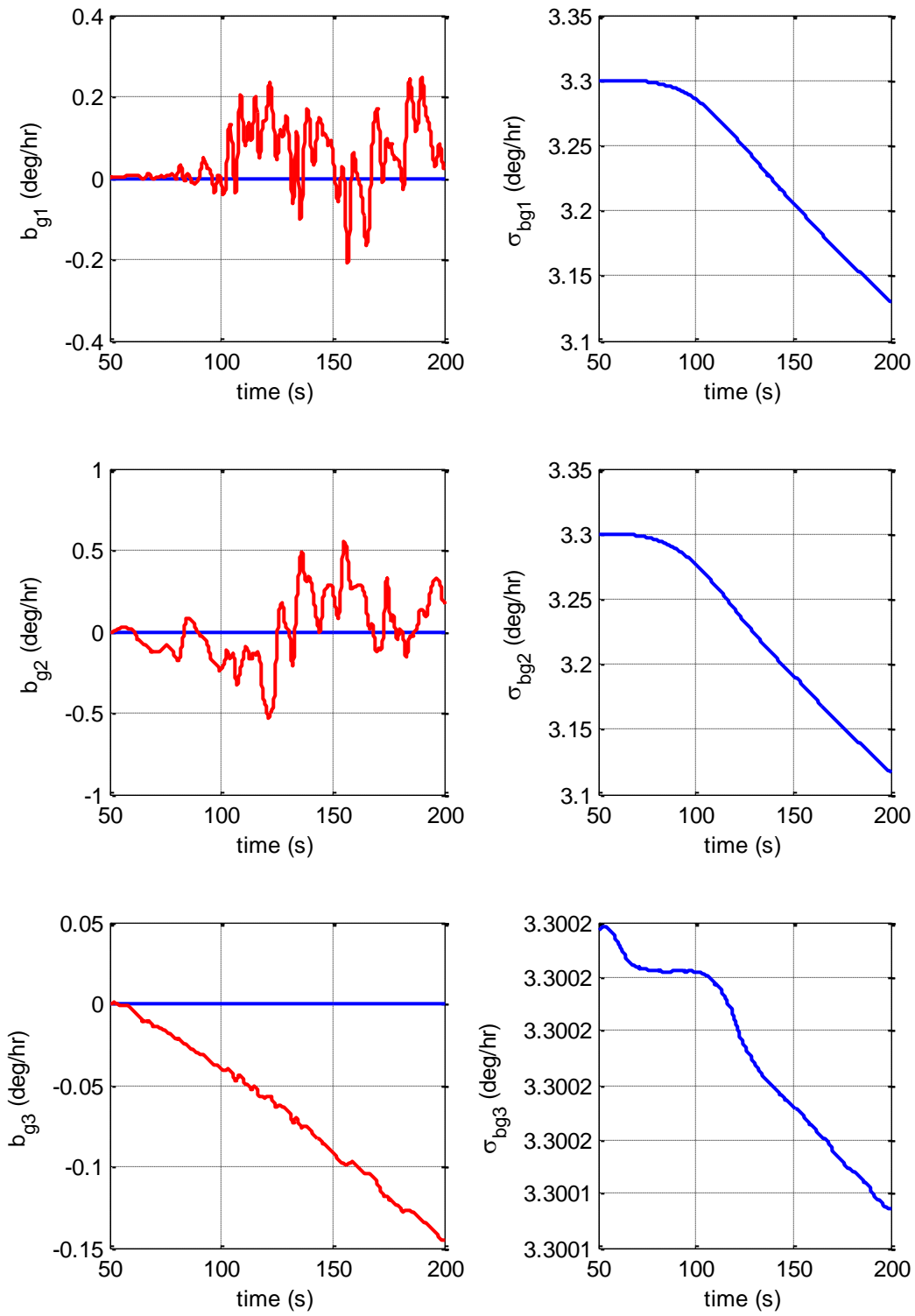


Figure 8.11: Gyro bias estimate and uncertainty versus time with LIDAR.

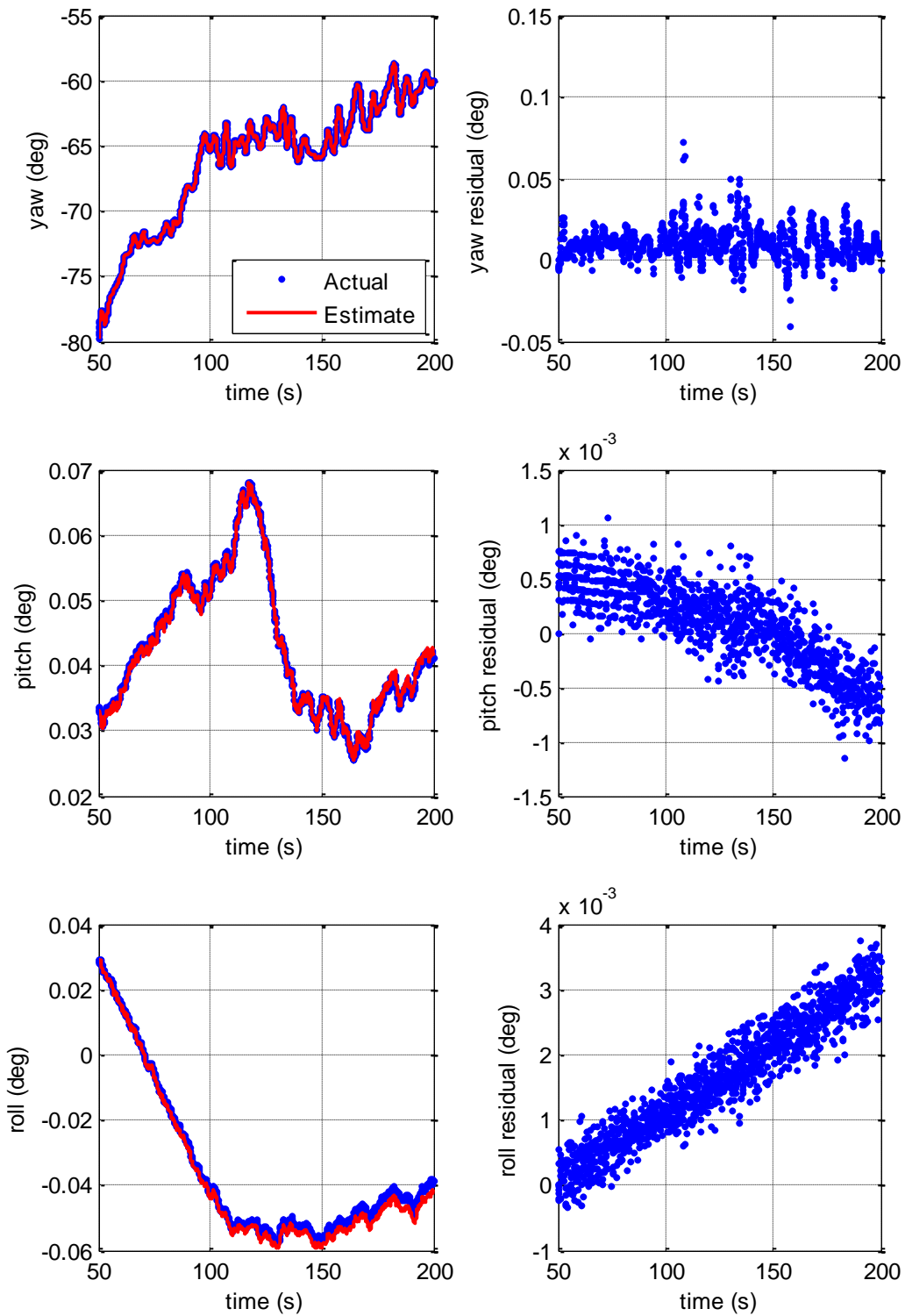


Figure 8.12: Attitude estimate and residual versus time without LIDAR.

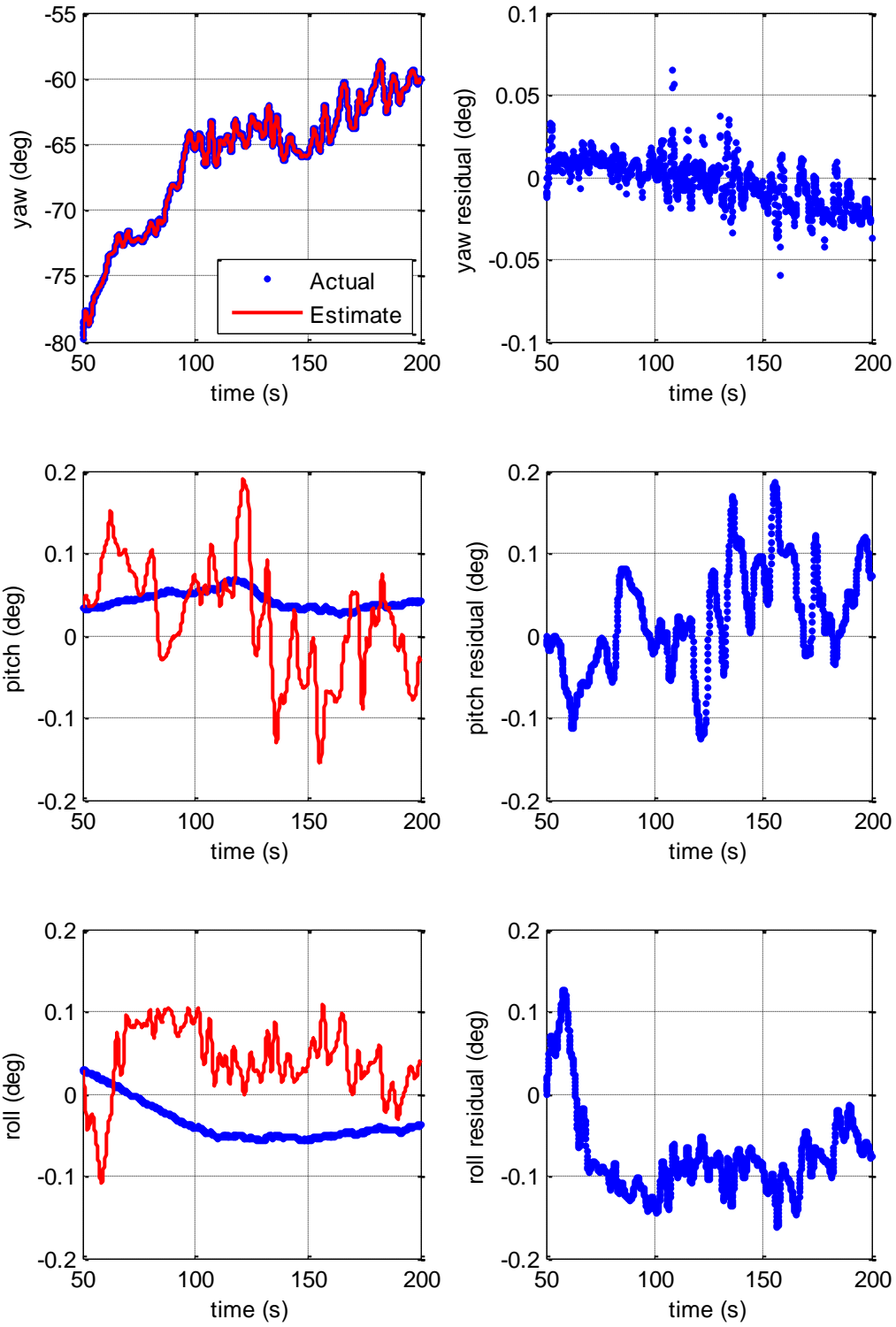


Figure 8.13: Attitude estimate and residual versus time with LIDAR.

9 Conclusion and Future Work

An algorithm for accurately estimating spacecraft position, velocity, and attitude during landing has been presented. The proposed estimator combines IMU-measured acceleration and angular velocity with LIDAR range and range-rate measurements in an extended Kalman filter framework to significantly enhance state estimation. Overall, filter results from a helicopter flight test are in excellent agreement with GPS data. Of particular note is that the new LIDAR system is orders of magnitude more accurate than existing flight-proven navigation systems that rely exclusively on IMU measurements.

Lessons garnered from this study will prove to be valuable in the development of the next prototype of the LIDAR system, scheduled to be tested in a series of flights in 2010. In addition, demonstration of this new pinpoint landing technology has direct relevance to future space missions, including Lunar South Pole/Aitken Basin Sample Return, Comet/Asteroid Surface Sample Return, Venus In-Situ Explorer, Mars Sample Return, Europa Lander, Titan Explorer, as well as human exploration missions to the Moon and Mars (Amzajerjian).

Recommendations for further work include: improving the LIDAR signal processing algorithm, such that data from the entire flight test can be used; improving the filtering and smoothing of the IMU data to remove the effects of high-frequency structural noise, measurement noise, and sensor quantization; fine-tuning the Kalman filter (or, alternatively, developing an algorithm for automatic tuning); developing a more sophisticated gravity model for the site of the flight test; and using a fourth-order Runge-

Kutta integrator in the filter update instead of the Euler method. Moreover, it may prove fruitful to perform a study of the optimal LIDAR geometry, i.e. adjusting the polar angle of the laser beams with respect to the vehicle z -axis. Perhaps most importantly, an emphasis is made here that no attempt be made to maintain nadir-lock with the LIDAR shroud during the next flight test. The LIDAR system should be fixed with respect to the vehicle, such that the actual orientation of the body is measured.

References

Amzajerjian, F. (PI), "New Millennium Program Space Technology-9," NASA Research Announcement NNH04ZSS002N, 2004.

Bennett, F.V, and Price, T.G., "Study of Powered-Descent Trajectories for Manned Lunar Landings," NASA Technical Note D-2426, 1964.

Chatfield, A.B., *Fundamentals of High Accuracy Inertial Navigation*, American Institute of Aeronautics and Astronautics, Inc., Reston, VA, 1997.

Farrenkopf, R.L., "Analytic Steady-State Accuracy Solutions for Two Common Spacecraft Attitude Estimators," *Journal of Guidance and Control*, Vol. 1, No. 4, 1978, pp. 282-284.

Lefferts, E.J., Markley, F.L., and Shuster, M.D., "Kalman Filtering for Spacecraft Attitude Estimation," *Journal of Guidance, Control, and Dynamics*, Vol. 5, No. 5, 1982, pp. 417-429.

Majji, M., and Mortari, D., "Quaternion Constrained Kalman Filter," *Advances in the Astronautical Sciences*, Vol. 130, No. 2, 2008, pp. 1717-1734.

Meirovitch, L., *Methods of Analytical Dynamics*, McGraw-Hill, New York, 1970.

Pierrottet, D., Amzajerjian, F., Petway, L., Barnes, B., and Lockard, G., "Flight Test Performance of a High Precision Navigation Doppler Lidar," NASA Technical Report LF99-8520, 2009.

Trawny, N., Mourikis, A.I., Roumeliotis, S.I., Johnson, A.E., and Montgomery, J.F., "Vision-Aided Inertial Navigation for Pin-Point Landing using Observations of Mapped Landmarks," *Journal of Field Robotics*, Vol. 24, No. 5, 2007, pp. 357-378.

Vallado, D.A., *Fundamentals of Astrodynamics and Applications*, Microcosm Press, Hawthorne, CA, 2007.

Wertz, J.R. (ed.), *Spacecraft Attitude Determination and Control*, D. Reidel Publishing Company, Boston, 1978.